

## The Galaxy Activity, Torus, and Outflow Survey (GATOS). VII. The 20–214 $\mu\text{m}$ imaging atlas of active galactic nuclei using SOFIA

LINDSAY FULLER,<sup>1</sup> ENRIQUE LOPEZ-RODRIGUEZ,<sup>2,3</sup> ISMAEL GARCÍA-BERNETE,<sup>4</sup> CRISTINA RAMOS ALMEIDA,<sup>5,6</sup>  
 ALMUDENA ALONSO-HERRERO,<sup>7</sup> CHRIS PACKHAM,<sup>1,8</sup> LULU ZHANG,<sup>1</sup> MASON LEIST,<sup>1</sup> NANCY LEVENSON,<sup>9</sup> MASA IMANISHI,<sup>8</sup>  
 SEBASTIAN HOENIG,<sup>10</sup> MARKO STALEVSKI,<sup>11,12</sup> CLAUDIO RICCI,<sup>13,14</sup> ERIN HICKS,<sup>15</sup> ENRICA BELLOCCHI,<sup>16,17</sup> FRANCOISE COMBES,<sup>18</sup>  
 RIC DAVIES,<sup>19</sup> SANTIAGO GARCÍA BURILLO,<sup>20</sup> OMAIRA GONZÁLEZ MARTÍN,<sup>21</sup> TAKUMA IZUMI,<sup>8</sup> ALVARO LABIANO,<sup>22</sup>  
 MIGUEL PEREIRA SANTAELLA,<sup>23</sup> DIMITRA RIGOPOLOU,<sup>4,24</sup> DAVID ROSARIO,<sup>25</sup> DANIEL ROUAN,<sup>26</sup> TARO SHIMIZU,<sup>19</sup> AND MARTIN WARD<sup>27</sup>

<sup>1</sup>University of Texas at San Antonio, One UTSA Circle, San Antonio, TX, 78249, USA

<sup>2</sup>Department of Physics & Astronomy, University of South Carolina, Columbia, SC 29208, USA

<sup>3</sup>Kavli Institute for Particle Astrophysics & Cosmology (KIPAC), Stanford University, Stanford, CA 94305, USA

<sup>4</sup>Department of Physics, University of Oxford, Keble Road, Oxford OX1 3RH, UK

<sup>5</sup>Instituto de Astrofísica de Canarias, Calle Vía Láctea, s/n, E-38205 La Laguna, Tenerife, Spain

<sup>6</sup>Departamento de Astrofísica, Universidad de La Laguna, E-38206 La Laguna, Tenerife, Spain

<sup>7</sup>Centro de Astrobiología (CAB), CSIC-INTA, Camino Bajo del Castillo s/n, E-28692 Villanueva de la Cañada, Madrid, Spain

<sup>8</sup>National Astronomical Observatory of Japan, National Institutes of Natural Sciences (NINS), 2-21-1 Osawa, Mitaka, Tokyo 181-8588, Japan

<sup>9</sup>Space Telescope Science Institute, 3700 San Martin Drive, Baltimore, MD 21218, USA

<sup>10</sup>School of Physics & Astronomy, University of Southampton, Southampton SO17 1BJ, UK

<sup>11</sup>Astronomical Observatory, Volgina 7, 11060 Belgrade, Serbia

<sup>12</sup>Sterrenkundig Observatorium, Universiteit Gent, Krijgslaan 281-S9, Gent B-9000, Belgium

<sup>13</sup>Núcleo de Astronomía de la Facultad de Ingeniería, Universidad Diego Portales, Av. Ejército Libertador 441, Santiago, Chile

<sup>14</sup>Kavli Institute for Astronomy and Astrophysics, Peking University, Beijing 100871, People's Republic of China

<sup>15</sup>Department of Physics and Astronomy, University of Alaska Anchorage, Anchorage, AK 99508-4664, USA

<sup>16</sup>Departamento de Física de la Tierra y Astrofísica, Fac. de CC Físicas, Universidad Complutense de Madrid, E-28040 Madrid, Spain

<sup>17</sup>Instituto de Física de Partículas y del Cosmos IPARCOS, Fac. CC Físicas, Universidad Complutense de Madrid, E-28040 Madrid, Spain

<sup>18</sup>LERMA, Observatoire de Paris, Collège de France, PSL University, CNRS, Sorbonne University, Paris, France

<sup>19</sup>Max Planck Institut für Extraterrestrische Physik, Giessenbachstrasse 1, D-85748 Garching bei München, Germany

<sup>20</sup>Observatorio de Madrid, OAN-IGN, Alfonso XII, 3, E-28014 Madrid, Spain

<sup>21</sup>Instituto de Radioastronomía y Astrofísica (IRyA), Universidad Nacional Autónoma de México, Antigua Carretera a Pízcuaro #8701, ExHda. San José de la Huerta, Morelia, Michoacán, C.P. 58089, Mexico

<sup>22</sup>Telespazio UK for the European Space Agency, ESAC, Camino Bajo del Castillo s/n, E-28692 Villanueva de la Cañada, Spain

<sup>23</sup>Instituto de Física Fundamental, CSIC, Calle Serrano 123, E-28006 Madrid, Spain

<sup>24</sup>School of Sciences, European University Cyprus, Diogenes street, Engomi, 1516 Nicosia, Cyprus

<sup>25</sup>School of Mathematics, Statistics and Physics, Newcastle University, Newcastle upon Tyne NE1 7RU, UK

<sup>26</sup>LESIA, Observatoire de Paris, Université PSL, CNRS, Sorbonne Université, Sorbonne Paris Citéé, 5 place Jules Janssen, F-92195 Meudon, France

<sup>27</sup>Centre for Extragalactic Astronomy, Department of Physics, Durham University, South Road, Durham DH1 3LE, UK

### ABSTRACT

We present a 19.7 – 214  $\mu\text{m}$  imaging atlas of local (4 – 181 Mpc; median 43 Mpc) active galactic nuclei (AGN) observed with FORCAST and HAWC+ on board the SOFIA telescope with angular resolutions  $\sim 3''$  –  $20''$ . This atlas comprises 22 Seyferts (17 Type 2 and 5 Type 1) with a total of 69 images, 41 of which have not been previously published. The AGN span a range of luminosities of  $\log_{10}(L_{\text{bol}}[\text{erg/s}]) = [42, 46]$  with a median of  $\log_{10}(L_{\text{bol}}[\text{erg/s}]) = 44.1 \pm 1.0$ . We provide total fluxes of our sample using aperture photometry for point source objects and a 2-D Gaussian fitting for objects with extended host galaxy emission, which was used to estimate the unresolved nuclear component. Most galaxies in our sample are point-like sources, however, four sources (Centaurus A, Circinus, NGC 1068, and NGC 4388) show extended emission in all wavelengths. The 30 – 40  $\mu\text{m}$  extended emission in NGC 4388 is coincident with the narrow line region at PA  $\sim 50^\circ$ , while the dusty extension at longer wavelengths arises from the host galaxy at PA  $\sim 90^\circ$ . Our new observations allow us to construct the best sampled spectral energy distributions (SEDs) available between 30 - 500  $\mu\text{m}$  for a sample of nearby AGN. We estimate that the average peak wavelength of the nuclear SEDs is  $\sim 40 \mu\text{m}$  in  $\nu F_\nu$ , which we associate with an unresolved extended dusty region heated by the AGN.

*Keywords:* galaxies — active galaxies — agn

## 1. INTRODUCTION

There is clear evidence that a considerable amount of dust in the vicinity of supermassive black holes (SMBHs) in active galaxies obscures the central engine (i.e., accretion disk and SMBH) in some lines of sight. Through spectropolarimetric observations of NGC 1068, Antonucci & Miller (1985) showed that its optical polarized spectrum contained broad optical polarized emission lines not originally observed by direct total intensity observations. It was subsequently presumed that an optically and geometrically thick dusty structure ('torus') blocked the central engine in some lines of sight (Antonucci 1993; Urry & Padovani 1995). Under this unified scheme a Type 1 AGN is seen face-on and shows broadened optical lines, while in Type 2 AGN the broadened lines are obscured. This model also predicts that broad silicate features at 10 and 18  $\mu\text{m}$  will be seen in emission in Type 1 and in absorption in Type 2. However, silicate emission can be seen in emission in some Type 2 AGN, while absorption can be seen in some Type 1 (e.g., Hatziminaoglou et al. 2015). This and other observational features are explained by the inhomogeneous nature of the torus. Clumpy torus models (Nenkova et al. 2008a,b) predict shallower silicate features, more similar infrared spectral energy distributions (SEDs) between Type 1 and Type 2 AGN, etc. (see Ramos Almeida & Ricci 2017, for a review).

A region of narrow forbidden line emission extends above and below the midplane of the dusty torus structure out to several kpc scales. Recent sub-arcsecond interferometric imaging observations have shown a dust component at pc-scales co-spatial with the base of the narrow line region (NLR; Hönig et al. 2012; Tristram et al. 2014; López-Gonzaga et al. 2014, 2016; Burtscher et al. 2013; Gámez Rosas et al. 2022; Isbell et al. 2022). This dusty structure is interpreted as part of a dusty wind launched from the inner hot part of the torus driven by radiation pressure at pc-scales (Hönig 2019), but generated by a magnetohydrodynamical wind at sub-pc scales (e.g., Emmering et al. 1992; Lopez-Rodriguez et al. 2015; Takasao et al. 2022; Lopez-Rodriguez et al. 2023). This extended dusty structure has been resolved in a nearby galaxy, ESO 418-G14, using mid-infrared (MIR) images with JWST/MIRI finding that the dust is primarily heated by the AGN and/or radiative jet-induced shocks in the NLR rather than a wind (Haidar et al. 2024).

ALMA observations provide observational support for a dusty torus+outflow scenario. Emission from the nucleus of NGC 1068 was mapped with a resolution of  $\sim 4$  pc, resolving a 7 – 10 pc diameter disk interpreted as the sub-mm counterpart of the torus (García-Burillo et al. 2016). Rotation of the compact emission was detected in HCN J=3-2 and HCO+ J=3-2 (Imanishi et al. 2018, 2020). A molecular outflowing wind co-spatial with the dusty and molecular torus was also observed (García-Burillo et al. 2019). Alonso-Herrero et al. (2018) interpreted the measured nuclear (10 – 20 pc)

CO(2-1) emission in NGC 5643 as a nuclear molecular gas component of the torus that is likely collimating the ionization cone. Conditions favorable for launching a cold and molecular wind likely depend on Eddington ratio and nuclear hydrogen column densities (e.g., Venanzi et al. 2020; García-Burillo et al. 2021; Alonso-Herrero et al. 2021; García-Bernete et al. 2022a).

This pc-scale dusty component is possibly associated with larger scale MIR emission detected out to 100s pc scales. In the case of Circinus, high angular resolution MIR imaging, optical polarimetry and integral field spectra, coupled with state-of-the-art radiative transfer simulations, provide evidence that extended dust emission from pc to tens of pc scales in this object is a result of a hollow dusty cone illuminated by a tilted accretion disk (Stalevski et al. 2017, 2019, 2023; Kakkad et al. 2023). MIR extended emission out to 1" ( $\sim 75$  pc) was clearly detected in NGC 1068 by Bock et al. (2000). Later 10.8 and 18.2  $\mu\text{m}$  emission extending 3"5 ( $\sim 200$  pc) across NGC 4151 was also attributed to dust in the NLR heated by the central engine (Radomski et al. 2003). Likewise, at similar wavelengths, extended emission in 18 AGN at distances out to hundreds of parsecs was detected (Asmus et al. 2016; García-Bernete et al. 2016; Asmus 2019). Using the 37.1  $\mu\text{m}$  filter on SOFIA/FORCAST and thanks to the increase in angular resolution compared with *Spitzer*, extended dust emission in Mrk 3, NGC 4151, and NGC 4388 was found on  $\sim 100$ s pc-scales (Fuller et al. 2019) coincident with the NLR and radio axis. This emission may be due to dust along the wall of ionization cones (Mason et al. 2009) or a dusty NLR (Mor et al. 2009; Mor & Netzer 2012).

In this manuscript we present an imaging atlas of 22 local ( $D = 4 - 181$  Mpc; median 42.8 Mpc) AGN obtained using the FORCAST and HAWC+ instruments on the 2.7-m SOFIA telescope in the wavelength range 20 – 214  $\mu\text{m}$ . Most of these datasets are unpublished or dispersed throughout the literature. We provide a mid- to far-IR imaging atlas at angular scales of  $\sim 3 - 20''$ . At these scales, contribution from several dust sources is expected and we expect to disentangle the emission sources in a future study. Instead, here we aim to determine whether these objects are extended or not, and at what wavelengths within the resolution of the SOFIA telescope. We also explore the wavelength of turnover in the SED. This atlas is complementary to JWST observations up to  $\sim 25 \mu\text{m}$  and archival *Herschel* data (70 – 500  $\mu\text{m}$ ).

The manuscript is organized as follows. Section 2 describes the observations and AGN sample definition; Section 3 shows the new IR images; Section 4 contains details of the imaging analysis and Section 5 shows the resulting SEDs; we present results about the data in Section 6.

## 2. AGN SAMPLE AND OBSERVATION DATA

### 2.1. Sample Selection

This imaging atlas was drawn from the ongoing AGN survey performed by the Galactic Activity, Torus, and Out-

flow Survey (GATOS; García-Burillo et al. 2021; Alonso-Herrero et al. 2021; García-Bernete et al. 2024). GATOS<sup>1</sup> aims to characterize the dynamics and composition of the dusty and molecular torus and multi-phase outflows in AGN. The GATOS parent sample is selected from the 70 Month *Swift*/BAT AGN catalog, which is flux limited in the ultra-hard 14 – 195 keV X-rays band (Baumgartner et al. 2013).

In the initial study of AGN using SOFIA observations (Fuller et al. 2016), sources from the GATOS survey were selected based on the criteria that the galaxies had been previously studied using CLUMPY (Nenkova et al. 2008a,b) torus models and were well-sampled in the 1 – 18  $\mu\text{m}$  regime (Ramos Almeida et al. 2009, 2011; Alonso-Herrero et al. 2011). The study of the 11 objects included the 31.5  $\mu\text{m}$  photometry in the SEDs and found that including the 31.5  $\mu\text{m}$  photometry reduces the number of CLUMPY torus models that are compatible with the data and modifies the model output for the torus outer radius. Fuller et al. (2019) further extended the wavelength range of a subset of 7 AGN SEDs to 37.1  $\mu\text{m}$ . They subsequently found extended emission in the PSF-subtracted images of Mrk 3, NGC 4151, and NGC 4388 that is coincident with the radio axis and NLR. In a separate study, Lopez-Rodriguez et al. (2018) modeled the torus of NGC 1068 using  $\sim 20 - 53 \mu\text{m}$  FORCAST and HAWC+ observations. They showed that the peak wavelength range of emission from the torus is  $\sim 30 - 40 \mu\text{m}$  with a characteristic temperature 70 - 100 K. The use of observations  $\gtrsim 30 \mu\text{m}$  in that study from SOFIA and ALMA highlights the importance of longer wavelength observations to put constraints on MIR emission sources. Based on these results, we extend the wavelength range in objects previously observed, and also expand the number of AGN observed.

We present the complete imaging atlas of 22 Seyferts observed by SOFIA in the wavelength range 19.7 – 214  $\mu\text{m}$  using FORCAST and HAWC+. The final set of observations presented here was part of a multi-year AGN survey over several observing SOFIA cycles (Proposal IDs: 02\_0035, 04\_0048, 06\_0066, 08\_0014; PI: Lopez-Rodriguez; 70\_0400 PI: Herter). The SOFIA atlas of AGN in the far-IR (FIR) is a flux-limited sample of nearby, bright, and well-studied AGN. All objects have a point source flux of  $> 200 \text{ mJy}$  at 31.5  $\mu\text{m}$ , which ensures that each band can be observed within 1 hr of on-source time with a signal to noise ratio  $> 10$  using FORCAST/SOFIA. Although the original AGN sample is larger than that presented here, only 22 AGN were observed in total by SOFIA before end of operations in 2022. Note that there are gaps in the 20 – 214  $\mu\text{m}$  wavelength range due to the fact that SOFIA only flies with a single instrument per night. For each SOFIA cycle, we prioritized the objects with observations acquired in a single instrument from the previous cycle.

The sample properties are given in Table 1. For most objects, we retrieved redshift data from the NASA Extragalactic Database (NED). However, for nearby objects Centaurus A

**Table 1.** SOFIA AGN Sample

Object	Type	$z$	Dist. (Mpc)	Scale (pc/ $''$ )	$\log L_{\text{Bol}}$ (erg s $^{-1}$ )	Refs.
CentaurusA	RLSy2	0.0018	3.8	17	44.0	a
Circinus	Sy2	0.0014	4.2	19	43.6	b
MCG-5-23-16	Sy2	0.0085	36.4	177	44.4	c
Mrk 3	Sy2	0.0135	57.9	280	45.1	d
Mrk 231	ULIRG/	0.0422	181	877	45.9	e
	Sy1					
Mrk 573	Sy2	0.0172	73.7	357	44.4	b
NGC 1068	Sy2	0.0038	16.3	79	45.0	f
NGC 1275	RG/	0.0176	75.4	366	44.8	g
	Sy1.5					
NGC 2110	Sy2	0.0076	32.6	158	43.9	b
NGC 2273	Sy2	0.0061	26.1	127	43.9	b
NGC 2992	Sy1.9	0.0077	33.0	160	43.5	h
NGC 3081	Sy2	0.0080	34.2	166	44.2	b
NGC 3227	Sy1.5	0.0038	16.3	79	43.3	i
NGC 3281	Sy2	0.0107	45.9	222	43.8	b
NGC 4151	Sy1.5	0.0033	14.1	69	43.9	f
NGC 4258	Sy2	0.0015	6.4	31	42.0	j
NGC 4388	Sy2	0.0047	20.1	98	44.7	d
NGC 4941	Sy2	0.0037	15.9	77	42.2	k
NGC 5506	Sy1.9	0.0062	26.6	129	44.3	b
NGC 7465	Sy2/	0.0066	28.1	136	43.4	k
	LINER					
NGC 7469	Sy1	0.0163	69.9	339	44.6	i
NGC 7674	Sy2	0.0290	124.3	603	45.5	b

Redshifts and spectral type were taken from NED. Distances to most sources were obtained using  $H_0 = 70 \text{ km s}^{-1} \text{ Mpc}^{-1}$ . Distances to nearby sources Centaurus A and Circinus were taken from Harris et al. (2010) and Tully et al. (2009), respectively.

References for  $\log L_{\text{bol}}$ : a) Borkar et al. (2021) b) Marinucci et al. (2012) c) Alonso-Herrero et al. (2011) d) Ichikawa et al. (2017), e) Leighly et al. (2014) f) Marconi et al. (2004), g) Baumgartner et al. (2013), h) García-Bernete et al. (2015), i) Ramos Almeida et al. (2011), j) Yuan et al. (2002), k) Duras et al. (2020),

and Circinus, distances were obtained individually (Harris et al. 2010; Tully et al. 2009). The 22 objects in this atlas cover the luminosity range of  $\log_{10}(L_{\text{bol}}[\text{erg/s}]) = [42, 46]$  with a median of  $\log_{10}(L_{\text{bol}}[\text{erg/s}]) = 44.1 \pm 1.0$ , and a distance of 4 – 181 Mpc with a median of 42.8 Mpc. Figure 1 shows bolometric luminosity plotted against distance, where Seyfert 1 objects are shown as red triangles and Seyfert 2 objects are shown as purple stars.

## 2.2. SOFIA Observations and Data Reduction

### 2.2.1. FORCAST

FORCAST is an IR camera and spectrograph sensitive in the wavelength range 5 – 40  $\mu\text{m}$  with a field of view (FOV) of  $3.4' \times 3.2'$  and pixel scale  $0.768''/\text{pixel}$ . With one exception (NGC 1068 in the 19.7  $\mu\text{m}$  filter), we only used the Long Wavelength Camera (LWC; 25 – 40  $\mu\text{m}$ ) due to the abundance of ground-based images at shorter wavelengths for the objects in our sample. FORCAST observations were made in dual channel mode using the two-position chop-nod (C2N) method with symmetric nod-match-chop (NMC) to remove telescope thermal emission and time variable sky background, and to reduce the effect of  $1/f$  noise from the array. Data were reduced by the SOFIA Science Center using the FORCAST\_REDUX pipeline following the methods described by Herter et al. (2012). Most of the pipeline changes over the

<sup>1</sup> GATOS website: <https://gatos.myportfolio.com/>

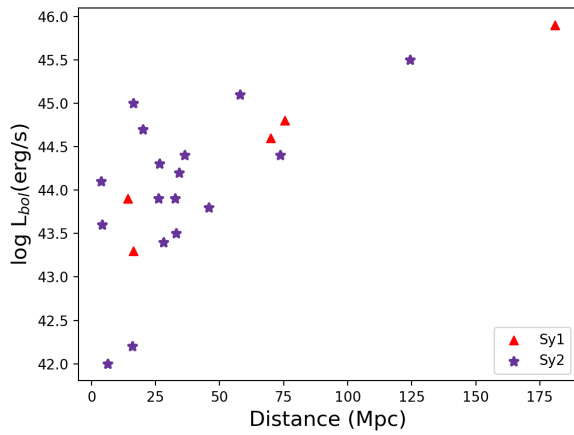


**Figure 1.** Luminosity plotted against distance of the 22 AGN in the atlas. Red triangles represent Sy1 and purple stars represent Sy2.

cycles were to refine the spectroscopic mode of FORCAST with little or no change to the image mode presented here.

Observations were flux-calibrated using the set of standard stars of the observing run, which provides flux uncertainties of  $\sim 10\%$ . The point spread function (PSF) of the  $31.5\text{ }\mu\text{m}$  observations from Cycle 2 (see Fuller et al. 2016) was the co-average of a set of standard stars from that cycle. Its FWHM was  $3.40''$ , in agreement with the SOFIA Observer’s Handbook v3.0.0. The PSFs for Cycle 4 in the  $30 - 40\text{ }\mu\text{m}$  wavelength range were determined by using standard star observations from the individual flights (see Fuller et al. 2019) and averaged at FWHM  $\sim 4.33''$  and  $4.58''$  in the  $31.5$  and  $37.1\text{ }\mu\text{m}$  filters, respectively. The FORCAST PSFs for the observations of NGC1068 are detailed in Lopez-Rodriguez et al. (2018).

### 2.2.2. HAWC+

HAWC+ is a FIR imaging polarimeter designed to allow total and polarized intensity imaging observations in four broad bands centered at  $53$ ,  $89$ ,  $155$ , and  $214\text{ }\mu\text{m}$ , corresponding to Bands A, C, D, and E respectively (see Table 2). On-

the-fly mapping (OTFMAP) observing modes were used for both imaging polarimetry and total intensity imaging. Observing modes for the individual observations are given in Table 3. Data taken in polarization mode was reduced using the HAWC\_DPR PIPELINE and the reduction steps presented in Lopez-Rodriguez et al. (2022b). The Comprehensive Reduction Utility for SHARC II (CRUSH; Kovács et al. 2006; Kovács 2008) was used to obtain the total intensity observations. HAWC+ observations were reduced following the same reduction steps. We quote the pipeline versions or CRUSH versions in Table 3 to differentiate between the observing modes. There are no differences between CRUSH versions to obtain the total intensity images as all the changes in the pipeline were done for the polarimetric mode. Table 3 also shows the pixel scale of each image.

**Table 2.** HAWC+ filter suite

Filter	$\lambda_{central}\text{ }(\mu\text{m})$	$\Delta\lambda\text{ }(\mu\text{m})$	FWHM ( $''$ )
Band A	53	8.7	4.85
Band C	89	17	7.8
Band D	154	34	13.6
Band E	214	44	18.2

As in FORCAST observations, the source of uncertainty in the photometry for HAWC+ results from calibration factors of the standard stars associated with the observation, giving an uncertainty of  $\sim 10\%$  (Lopez-Rodriguez et al. 2022b). HAWC+ PSFs were estimated using standard star observations in 2017. Pallas was observed in Bands A and C on 7 November 2017, while Neptune was observed in Bands D and E on 19 October, 2017. The FWHM of these standards are  $5.25''$ ,  $8.26''$ ,  $14.74''$ , and  $19.65''$  in Bands A, C, D, and E, respectively. The FWHMs from the Observer’s Handbook<sup>2</sup> are given in Table 2.

### 2.3. Observing Data

Table 3 provides the final AGN sample with information about the wavelength, observing mode, observation and mission details, versions of the separate pipelines, and also the field-of-view (FOV) of the individual images.

<sup>2</sup> <https://irsa.ipac.caltech.edu/data/SOFIA/docs/sites/default/files/Other/Documents/OH-Cycle7.pdf>

**Table 3.**

Object	Wavelength ( $\mu\text{m}$ )	Instrument	Date	Observing mode	Pipeline/ CRUSH vers.	On-source time (s)	Altitude (ft)	Mission ID	Program ID	Image FOV (arcsec $^2$ )	Pixel scale (")
Centaurus A	53	HAWC+	2019-07-17	polarization	2.3.2	428	39022	HA_F597	07_0032	75"×75"	1.29
	89	HAWC+	2019-07-17	polarization	2.3.2	856	39020	HA_F597	07_0032	130"×130"	2.02
Circinus	53	HAWC+	2019-07-16	polarization	2.3.2	107	42014	HA_F596	07_0032	70"×70"	1.00
	89	HAWC+	2019-07-16	polarization	2.3.2	856	40994	HA_F596	07_0032	105"×105"	2.00
	215	HAWC+	2019-07-16	polarization	2.3.2	281	43011	HA_F596	07_0032	140"×140"	4.72
MCG-5-23-16	31.5	FORCAST	2014-05-03	imaging	1.0.IBeta	324	38076	FO_F167	02_0035	20"×20"	0.77
	53	HAWC+	2018-07-04	tot. intensity	CSH 2.41-3	321	39996	HA_F480	06_0066	50"×50"	1.00
	89	HAWC+	2018-07-04	tot. intensity	CSH 2.41-3	321	40003	HA_F480	06_0066	75"×75"	1.55
	155	HAWC+	2018-07-04	tot. intensity	CSH 2.41-3	642	39991	HA_F480	06_0066	90"×90"	2.75
Mrk 3	31.5	FORCAST	2016-09-27	imaging	1.1.3	35	42994	FO_F133	04_0048	20"×20"	0.77
	37.1	FORCAST	2016-09-27	imaging	1.1.3	43	43002	FO_F133	04_0048	20"×20"	0.77
	53	HAWC+	2018-09-21	tot. intensity	CSH 2.41-3	1926	43002	HA_F508	06_0066	50"×50"	1.00
	89	HAWC+	2019-02-13	tot. intensity	CSH 2.41-3	1277	43015	HA_F546	06_0066	75"×75"	1.55
Mrk 231	155	HAWC+	2019-02-13	tot. intensity	CSH 2.41-3	766	43003	HA_F546	06_0066	90"×90"	2.75
	89	HAWC+	2019-09-18	polarization	2.3.2	749	40010	HA_F611	07_0032	75"×75"	2.00
Mrk 573	31.5	FOR	2015-02-05	imaging	1.0.3	384	40008	FO_F192	02_0035	20"×20"	0.77
	37.1	FOR	2018-09-08	imaging	1.3.2	31	43006	FO_F502	06_0066	20"×20"	0.77
NGC 1068	19.7	HAWC+	2016-09-17	imaging	1.1.3	427	42980	FO_F329	70_0400	30"×30"	0.77
	31.5	HAWC+	2016-09-17	imaging	1.1.3	471	42980	FO_F329	70_0400	40"×40"	0.77
NGC 1275	31.5	FORCAST	2016-09-21	imaging	1.1.3	343	42980	FO_F329	70_0400	40"×40"	0.77
	37.1	FORCAST	2016-09-21	imaging	1.1.3	40012	HA_F356	70_0409	60"×60"	1.00	
NGC 2110	89	HAWC+	2017-10-20	polarization	2.7.0	1364	40018	HA_F443	08_0012	10"×60"	4.02
	31.5	FORCAST	2016-09-21	imaging	1.1.3	48	41103	FO_F274	04_0048	20"×20"	0.77
NGC 2110	37.1	FORCAST	2019-09-05	polarization	2.3.2	7680	40021	HA_F606	07_0032	50"×50"	1.55
	89	HAWC+	2015-02-05	imaging	1.0.3	768	38001	FO_F192	02_0035	20"×20"	0.77

**Table 3** *continued*

**Table 3 (continued)**

53	HAWC+	2018-09-28	tot. intensity	CSH 2.41-3	642	42984	HA_F512	06_0066	50"×50"	1.00
89	HAWC+	2018-09-28	tot. intensity	CSH 2.41-3	320	42945	HA_F512	06_0066	75"×75"	1.55
155	HAWC+	2018-09-28	tot. intensity	CSH 2.41-3	320	42955	HA_F512	06_0066	90"×90"	2.75
215	HAWC+	2018-09-28	tot. intensity	CSH 2.41-3	320	42945	HA_F512	06_0066	90"×90"	3.70
NGC 2273	31.5	FORCAST	2016-09-27	imaging	1.1.3	34	42998	FO_F333	04_0048	20"×20"
37.1	FORCAST	2016-09-27	imaging	1.1.3	41	42996	FO_F333	04_0048	20"×20"	0.77
53	HAWC+	2018-09-28	tot. intensity	CSH 2.41-3	428	38987	HA_F512	06_0066	50"×50"	1.00
89	HAWC+	2018-09-28	tot. intensity	CSH 2.41-3	534	38949	HA_F512	06_0066	75"×75"	1.55
155	HAWC+	2018-09-28	tot. intensity	CSH 2.41-3	321	38956	HA_F512	06_0066	90"×90"	2.75
215	HAWC+	2018-09-28	tot. intensity	CSH 2.41-3	321	38960	HA_F512	06_0066	90"×90"	3.70
NGC 2992	31.5	FORCAST	2014-05-02	imaging	1.0.1Beta	232	39026	FO_F166	02_0035	20"×20"
NGC 3081	31.5	FORCAST	2014-05-02	imaging	1.0.1Beta	480	39021	FO_F166	02_0035	20"×20"
37.1	FORCAST	2016-02-17	imaging	1.0.1Beta	63	43004	FO_F278	04_0048	20"×20"	0.77
NGC 3227	31.5	FORCAST	2014-05-06	imaging	1.0.1Beta	152	37990	FO_F168	02_0035	20"×20"
37.1	FORCAST	2016-02-17	imaging	1.1.0	35	43002	FO_F278	04_0048	20"×20"	0.77
NGC 3281	31.5	FORCAST	2014-05-02	imaging	1.0.1Beta	300	39033	FO_F166	02_0035	20"×20"
53	HAWC+	2018-07-12	tot. intensity	CSH 2.41-3	321	37036	HA_F485	06_0066	50"×50"	1.00
89	HAWC+	2018-07-12	tot. intensity	CSH 2.41-3	320	37025	HA_F485	06_0066	75"×75"	1.55
155	HAWC+	2018-07-12	tot. intensity	CSH 2.41-3	320	37043	HA_F485	06_0066	90"×90"	2.75
215	HAWC+	2018-07-12	tot. intensity	CSH 2.41-3	534	37049	HA_F485	06_0066	90"×90"	3.70
NGC 4151	31.5	FORCAST	2014-05-08	imaging	1.0.1Beta	153	40042	FO_F170	02_0035	20"×20"
37.1	FORCAST	2016-02-17	imaging	1.0.1Beta	41	36996	FO_F278	04_0048	20"×20"	0.77
53	HAWC+	2019-02-12	tot. intensity	CSH 2.41-3	1069	39777	HA_F545	06_0066	50"×50"	1.00
89	HAWC+	2019-02-12	polarization	2.3.2	891	40034	HA_F545	06_0066	75"×75"	1.55
NGC 4258	31.5	FORCAST	2016-02-17	imaging	1.1.0	156	39002	FO_F278	04_0048	30"×30"
37.1	FORCAST	2016-02-17	imaging	1.1.0	446	38999	FO_F278	04_0048	30"×30"	0.77
NGC 4388	31.5	FORCAST	2014-05-02	imaging	1.0.1Beta	162	37982	HA_F545	02_0035	20"×20"
37.1	FORCAST	2016-02-06	imaging	1.1.0	63	42372	FO_F274	04_0048	20"×20"	0.77
53	HAWC+	2019-02-12	tot. intensity	CSH 2.41-3	932	42045	HA_F545	06_0066	50"×50"	1.00
89	HAWC+	2019-02-12	tot. intensity	CSH 2.41-3	534	42035	HA_F545	06_0066	75"×75"	1.55

**Table 3 continued**

**Table 3** (*continued*)

	155	HAWC+	2019-02-12	tot. intensity	CSH 2.41-3	321	42021	HA_F545	06_0066	90°×90°	2.00
	215	HAWC+	2019-02-12	tot. intensity	CSH 2.41-3	213	42037	HA_F545	06_0066	90°×90°	3.70
NGC 4941	31.5	FORCAST	2021-04-09	imaging	2.21	154	38992	FO_F715	08_0014	20°×20°	0.77
	37.1	FORCAST	2021-04-09	imaging	2.21	313	38986	FO_F715	08_0014	20°×20°	0.77
NGC 5506	31.5	FORCAST	2014-05-02	imaging	1.0_IBeta	261	37982	FO_F166	02_0035	20°×20°	0.77
	37.1	FORCAST	2021-06-30	imaging	2.30	427	39005	FO_F752	08_0014	20°×20°	0.77
	89	HAWC+	2020-01-31	polarization	2.32	779	43009	HA_F657	07_0032	75°×75°	1.55
NGC 7465	31.5	FORCAST	2022-09-17	imaging	2.60	427	41017	FO_F915	08_0014	20°×20°	0.77
	37.1	FORCAST	2022-09-17	imaging	2.60	222	41009	FO_F915	08_0014	20°×20°	0.77
	53	HAWC+	2021-09-14	tot. intensity	CSH 2.42-1	641	38008	HA_F783	08_0014	20°×20°	1.00
	89	HAWC+	2021-09-14	tot. intensity	CSH 2.42-1	426	39004	HA_F783	08_0014	20°×20°	1.55
NGC 7469	31.5	FORCAST	2014-06-04	imaging	1.0_IBeta	231	43005	FO_F176	02_0035	20°×20°	0.77
NGC 7674	31.5	FORCAST	2014-06-04	imaging	1.0_IBeta	165	43005	FO_F176	02_0035	20°×20°	0.77

Note—Observation Data - Column 1: Object; Column 2: Wavelength; Column 3: Instrument; Column 4: Observation date; Column 5: Observing mode; Column 6: Pipeline/CRUSH version; Column 7: On-source time; Column 8: Aircraft starting altitude; Column 9: Mission ID; Column 10: Program ID; Column 11: FOV of images in Section 3; Column 12: Pixel scale

### 3. IMAGES

Images of the 22 AGN in the  $19.7 - 214 \mu\text{m}$  wavelength range are presented in Figures 2, 3, 4, and 5. The orange scale on the bottom left of the images indicates a scale of 500 pc. The beam size is depicted in white in the top right of the images. In all images, north is up and east is to the left. Complementary *Herschel*  $70 - 500 \mu\text{m}$  images are shown in Appendix A (Fig. 10, 11, 12, 13). These fully reduced images were obtained through the *Herschel* Science Archive<sup>3</sup>. All objects are presented and analyzed individually.

**Centaurus A.** The host galaxy of Centaurus A is clearly visible in the  $53 \mu\text{m}$  image with a bright compact center. However, the host galaxy becomes more dominant in the  $89 \mu\text{m}$  image (see a detailed analysis of host galaxy dust emission at  $89 \mu\text{m}$  in Lopez-Rodriguez 2021). The kpc-scale warped dust and gas lane was first observed with *Spitzer* imaging using IRAC and MIPS (Quillen et al. 2006). On subarcsecond scales, Radomski et al. (2008) observed the nucleus of Centaurus A using the  $8.8$ ,  $10.4$ , and  $18.3 \mu\text{m}$  filters on T-ReCS at Gemini South. They concluded that the mostly likely sources of nuclear MIR emission are an unresolved clumpy dusty torus in the core, and a dusty NLR for the arcsecond-scale extended emission (see also García-Bernete et al. 2016).

**Circinus Galaxy.** HAWC+  $53$  and  $89 \mu\text{m}$  images of the Circinus Galaxy show a very bright FIR core with extended emission at a PA  $\sim 30^\circ$ , whereas the  $215 \mu\text{m}$  image shows a slightly different PA  $\sim 55^\circ$ . We estimate the FWHM of the extended FIR nuclear emission to be  $\sim 6'' \times 6''$ ,  $13.5'' \times 11.5''$ , and  $22.3'' \times 25.6''$  at  $53$ ,  $89$ , and  $214 \mu\text{m}$ , respectively. These are larger than the PSF FWHMs given in Section 2.2.2, which indicates extended emission along the axis of the inner bar of the galaxy. MIR emission was resolved at  $8.7$  and  $18.3 \mu\text{m}$  out to  $2''$  in an approximate east-west direction, coincident with the ionization cones at PA  $\sim 100^\circ$  (Packham et al. 2005; Stalevski et al. 2017). However, the elongation seen in the SOFIA images (and in *Herschel* images in Appendix A) seems to be arising from dust in the host galaxy.

**MCG-5-23-16.** MCG-5-23-16 appears as a point-like source in the  $31.5 - 155 \mu\text{m}$  wavelength range whose brightness decreases with increasing wavelength. However, this galaxy appears as an extended source in the MIR using high angular resolution data from VLT (García-Bernete et al. 2016). Likewise, Ferruit et al. (2000) found that this nucleus has an extended optical NLR at a PA of  $40^\circ$ . They found a dust lane extending  $2''$  on either side of the nucleus, parallel to the axis of the galaxy. Their extended dusty emission at  $40^\circ$  was detected at a  $3\sigma$  level up to  $\sim 4''$  from the core. This extended structure has no thermal emission counterpart within the  $31.5 - 155 \mu\text{m}$  wavelength range.

**Mrk 3.** Although the FORCAST and HAWC+ images generally appear to be point-like sources, Fuller et al. (2019) found extended emission in the PSF-subtracted  $37.1 \mu\text{m}$  im-

age of Mrk 3 in the direction of the radio axis ( $84^\circ$ ; Kukula et al. 1993) and the NLR ( $\sim 70^\circ$ ; Capetti et al. 1995). Asmus et al. (2013) found an elongated nucleus out to  $\sim 170$  pc with PA  $\sim 70^\circ$  in the Si-5 ( $11.6 \mu\text{m}$ ) filter using Gemini/MICHELLE. However, the Si-2 ( $8.7 \mu\text{m}$ ) image from GTC/Canaricam appears point-like (Alonso-Herrero et al. 2016). The large scale east-west structure in the  $53 \mu\text{m}$  image here is a background artifact produced by the data reduction due to the small spatial coverage and short integration time of the observation.

**Mrk 231.** The  $89 \mu\text{m}$  image shown here is point-like with a FWHM of  $\sim 8.5''$ , similar to the standard FWHM of  $8.26''$  (see Section 2.2.2). Mrk 231 is a Type 1 Ultra Luminous Infrared Galaxy (ULIRG) and is the nearest known quasar at a distance of  $181 \text{ Mpc}$ . It is known for its multi-phase and multi-scale outflows (see Rupke & Veilleux 2011), with a neutral outflow up to  $3 \text{ kpc}$  in radius (Rupke et al. 2005). **Mrk 573.** Although the SNR is very low ( $3 - 4\sigma$ ), both  $31.5$  and  $37.1 \mu\text{m}$  images of Mrk 573 show marginally resolved  $\sim 4.5''$  elongation in the east-west direction at PA  $\sim 110^\circ$ . Mrk 573 was previously shown to have a biconical NLR coincident with radio emission  $3-4''$  from the nucleus at a PA  $\sim 125^\circ$  (Ulvestad & Wilson 1984; Pogge & De Robertis 1995). The marginal detection here may be cold extended dust in the outer layers of the NLR.

**NGC 1068.** The  $19 - 53 \mu\text{m}$  images of NGC 1068 were published previously in Lopez-Rodriguez et al. (2018), where it was shown that the peak emission from the torus occurs between  $30 - 40 \mu\text{m}$  with a corresponding temperature of  $70 - 100 \text{ K}$ . The  $89 \mu\text{m}$  image was published as a polarimetric observation (Lopez-Rodriguez et al. 2020). Within a scale of about  $1 \text{ kpc}$ , NGC 1068 shows extended emission in the NE to SW direction at a PA  $\sim 45^\circ$ , similar to MIR observations using VISIR/VLT (Asmus et al. 2014). Their observations revealed a nuclear structure in the north-south direction and extended structures to the NE and SW. From the N-band spectrum, Mason et al. (2006) concluded that while torus emission dominates NIR wavelengths, large-scale MIR emission is dominated by diffuse dust within the ionization cones.

**NGC 1275.** All  $30 - 53 \mu\text{m}$  images are dominated by a point-like source. However, the  $31.5 \mu\text{m}$  image (Fuller et al. 2019) shows  $3\sigma$  extended emission along the PA  $\sim 140^\circ$ . This AGN is known to have a network of H $\alpha$  filaments extending out to  $\sim 100''$  (see Conselice et al. 2001) and is possibly the result of a merger (Holtzman et al. 1992). The MIR core shows silicate dust emission in both  $10$  and  $18 \mu\text{m}$  bands (see Fuller et al. 2019). Hence, both dust and gas are extended covering several kpc around the core. In the HAWC+  $89 \mu\text{m}$  filter, Lopez-Rodriguez et al. (2023) found extended dust emission at a PA  $\sim 125^\circ$  out to a  $12 \text{ kpc}$  radius potentially associated with a magnetized dusty filament along the NW direction (Fabian et al. 2008).

**NGC 2110.** The  $30 - 215 \mu\text{m}$  images of NGC 2110 are all point-like. The north-south pattern in the  $53 \mu\text{m}$  image is due to background noise and does not represent extended dust. NGC 2110 is a Type 2 AGN that shows silicate emission at  $10$  and  $18 \mu\text{m}$  that is interpreted as a result of a clumpy torus, or as

<sup>3</sup>The *Herschel* archive can be found at <http://hercshel.esac.esa.int/ScienceArchive.shtml>

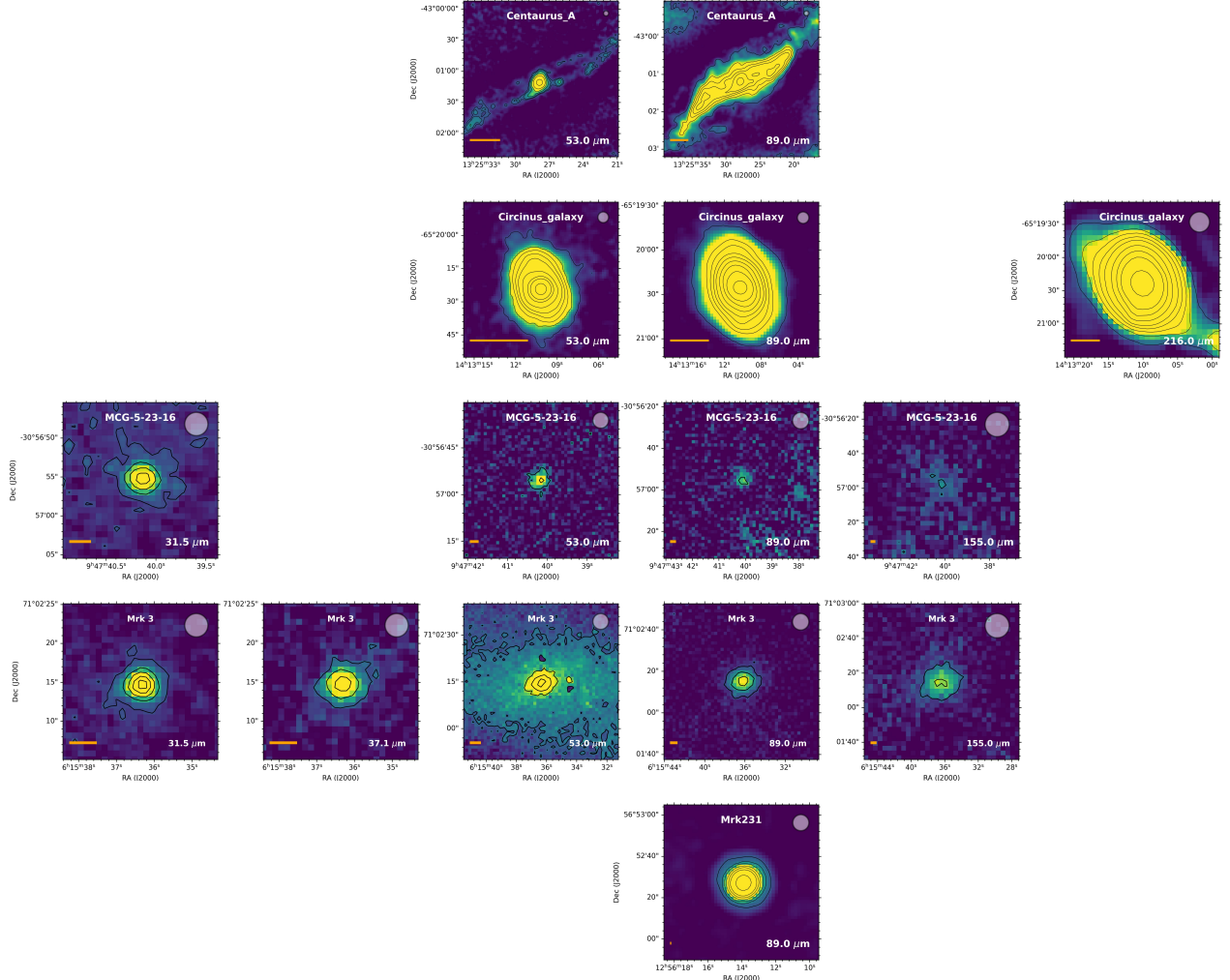


**Figure 2.** FORCAST 31.5, and 37.1  $\mu\text{m}$  images, and HAWC+ 53, 89, 155, and 215  $\mu\text{m}$  images. Each image has a differing FOV, which can be found in Table 3. For bright objects (Centaurus A, Circinus, and Mrk 231) contours start at  $3\sigma$ , then follow  $\log(\text{maximum})$  from [-1.2 to 0.8], [-1.8 to 0.8] [-1.4,0.8] in steps of 0.2. For MCG-5-23-16 and Mrk 3, the lowest contours are  $3\sigma$  and increase in steps of  $5\sigma$ . The white transparent circle on the top right indicates the telescope beam size. The orange bar on the bottom left of the images is scaled to 500 pc. For all images, north is up and east is to the left.

dust within the ionization cones ( $\text{PA} \sim 160^\circ$ ; [Mulchaey et al. 1994](#)) in the inner 32 pc of the AGN ([Mason et al. 2009](#)). This galaxy appears as an extended source in Gemini/MICHELLE high resolution N-band observations ([García-Bernete et al. 2016](#)). However, any structure within the NLR or ionization cones is not resolved by our observations.

**NGC 2273.** The full set of 30 - 215  $\mu\text{m}$  images of NGC 2273 show a point-like source. The north/south pattern in the 53  $\mu\text{m}$  image is due to background noise and does not represent extended dust. Within the FWHM of these images

(see Sections 2.2.1, 2.2.2), there is a known star-forming ring within  $\sim 2''$  of the nucleus ([Ferruit et al. 2000](#); [Martini et al. 2003](#); [Sani et al. 2012](#)). GTC/Canaricam observations ([Alonso-Herrero et al. 2014, 2016](#)) at 8.7  $\mu\text{m}$  show elongation from the north-east to the south-west, likely with contribution from PAH. This structure is consistent with extension seen in the PSF-subtracted 37.1  $\mu\text{m}$  SOFIA image ([Fuller et al. 2019](#)).

**NGC 2992.** The image of NGC 2992 in the 31.5  $\mu\text{m}$  filter is published in [Fuller et al. \(2016\)](#) and appears as a point-like source. Subarcsecond N-band imaging ([García-Bernete et al.](#)

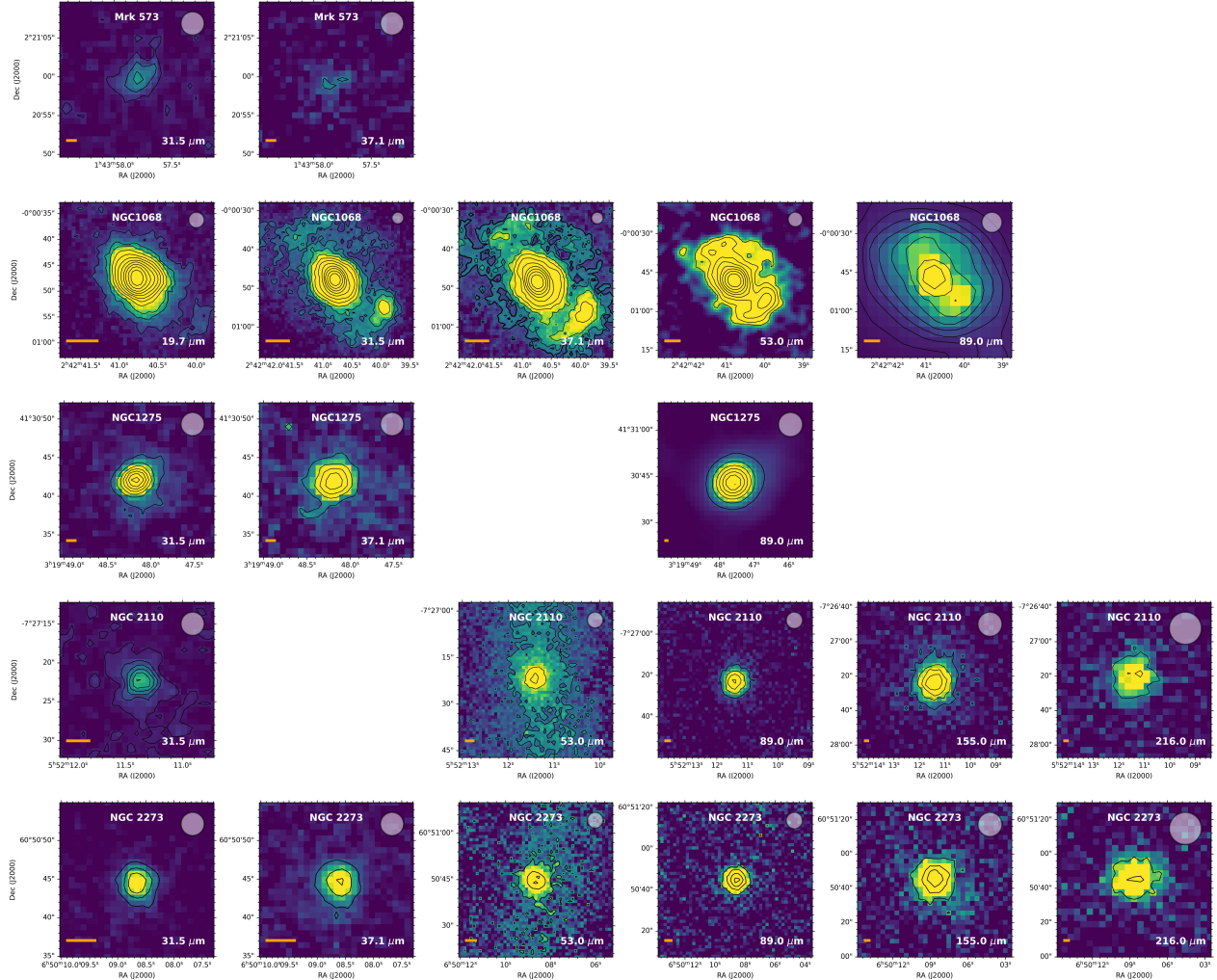


**Figure 3.** FORCAST 31.5 and 37.1  $\mu\text{m}$  images, and HAWC+ 53, 89, 155, and 215  $\mu\text{m}$  images. Note that the wavelength range for NGC 1068 starts 19.7  $\mu\text{m}$ , so its range is shifted. Each image has a differing FOV, which can be found in Table 3. For NGC 1068 FORCAST images, contours begin at  $3\sigma$  and follow  $\log(\text{maximum})$  from [-2.0,0.8] in steps of 0.2, while the HAWC+ images follow the same steps but  $\log(\text{max})$  ranges [-1.6,0.8]. For all other images, the lowest contours are  $3\sigma$  and increase in steps of  $5\sigma$ . The white transparent circle on the top right indicates the telescope beam size. The orange bar on the bottom left of the images is scaled to 500 pc. For all images, north is up and east is to the left.

2015) reveals extended emission along PA  $\sim 30^\circ$  out to  $\sim 3$  kpc which is attributed to dust heated by star formation based on corresponding N-band spectroscopy. The FWHM of the SOFIA image is  $\sim 3.5'' \times 3.5''$  ( $560 \times 560 \text{ pc}^2$ ) so the extension should be resolvable within the SOFIA image. Since we do not see the extension in the image here, we conclude that either the extended dust emission tapers at wavelengths  $\gtrsim 20 \mu\text{m}$  or SOFIA does not have enough sensitivity to detect it.

**NGC 3081.** The 31.5  $\mu\text{m}$  image of NGC 3081 was published in Fuller et al. (2016) while the 37.1  $\mu\text{m}$  image was

published in Fuller et al. (2019). The nucleus is known to harbor a region of strong optical emission  $\sim 1''$  from the AGN (Ferruit et al. 2000) likely due to dust or gas heated by the AGN. Fuller et al. (2019) estimated that  $\sim 35\%$  of the MIR emission within the central few arcseconds (few hundred parsecs) of the AGN originates in the NLR. High angular resolution N- and Q- band observations show extension towards the north, extending out to  $\sim 450$  pc from the south-east to the north-west (PA  $\sim 160^\circ$ ; García-Bernete et al. 2016). On larger scales, optical and NIR observations reveal a series of star

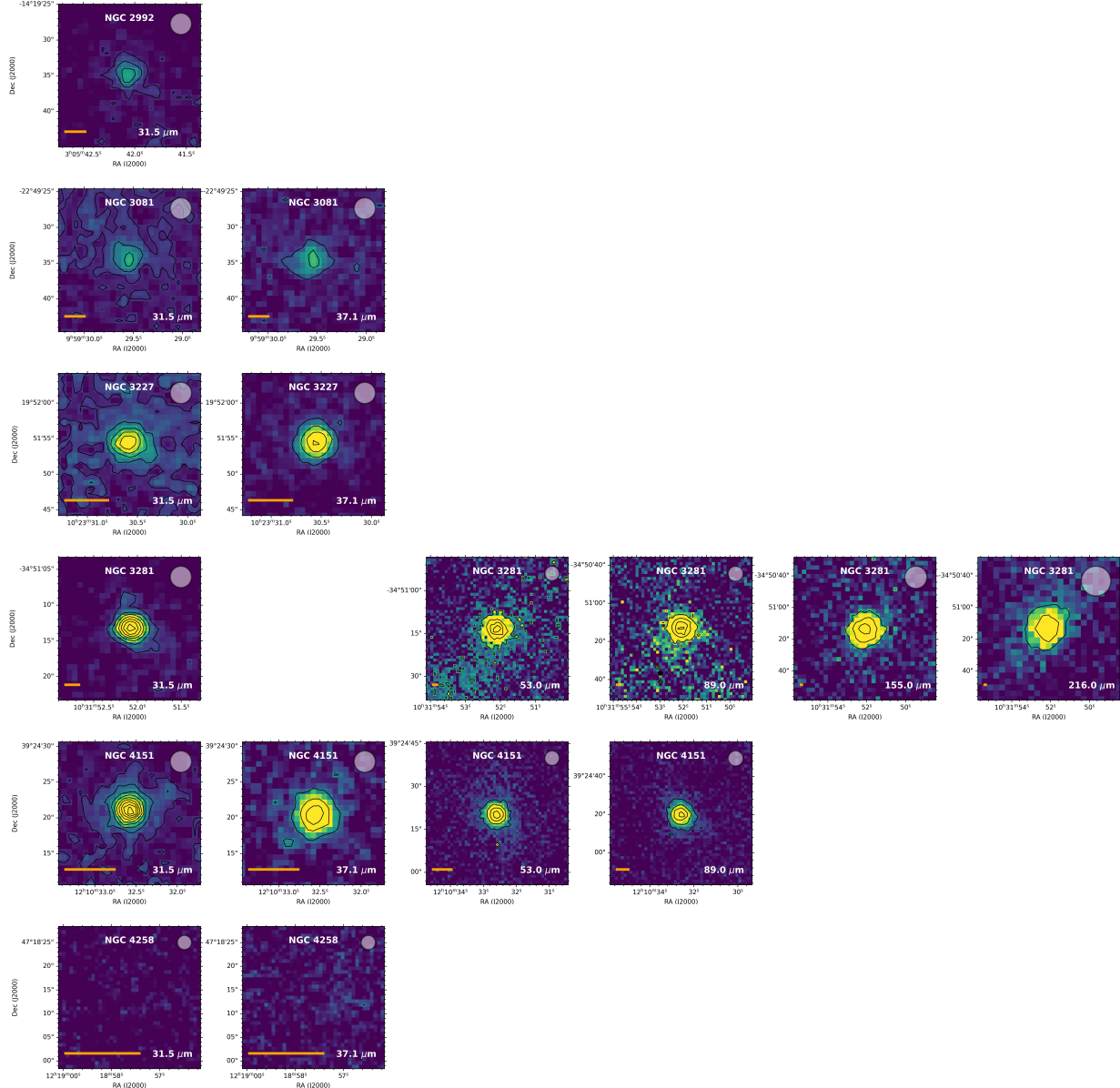


**Figure 4.** FORCAST 31.5 and 37.1  $\mu\text{m}$  images, and HAWC+ 53, 89, 155, and 215  $\mu\text{m}$  images. Each image has a differing FOV, which can be found in Table 3. The lowest contours are  $3\sigma$  and increase in steps of  $5\sigma$ . The white transparent circle on the top right indicates the telescope beam size. The orange bar on the bottom left of the images is scaled to 500 pc. For all images, north is up and east is to the left.

forming resonance rings at distances of 2.3, 11.0, 26.9 kpc and 33.1 kpc (Buta 1990; Buta et al. 1998, 2004). At longer wavelengths ( $\gtrsim 200 \mu\text{m}$ ), Ramos Almeida et al. (2011) concluded that FIR emission is contaminated by the star-forming ring 2.3 kpc in diameter.

**NGC 3227.** The 31.5  $\mu\text{m}$  image was published in Fuller et al. (2016) while the 37.1  $\mu\text{m}$  image was published in Fuller et al. (2019). These images show a point-like source, although NGC 3227 is known to harbor a nuclear star-forming region (Schinnerer et al. 2001; Davies et al. 2006) with a nuclear cluster within  $\sim 70$  pc ( $\sim 1''$ ) from the core. The 8.7  $\mu\text{m}$  image from Alonso-Herrero et al. (2016) shows a slight north/south elongation and the corresponding spectrum shows clear PAH

in the nucleus (see also García-Bernete et al. 2016). These star forming regions likely contaminate the nuclear MIR emission within the FWHM of our images.

**NGC 3281.** While the 31.5  $\mu\text{m}$  FORCAST image is published in Fuller et al. (2016), the HAWC+ images at 53, 89, 154, and 214  $\mu\text{m}$  are presented here for the first time and appear point-like in all filters. The images taken at 53 and 89  $\mu\text{m}$  appear to have significant noise in their backgrounds. The subarcsecond (0.35'') N-band spectrum in González-Martín et al. (2013) shows a deep 10  $\mu\text{m}$  silicate absorption feature which originates in the inner  $\sim 80$  pc of the AGN.

**NGC 4151.** The SOFIA images of NGC 4151 appear as a point-like source, with a potential detection of extended

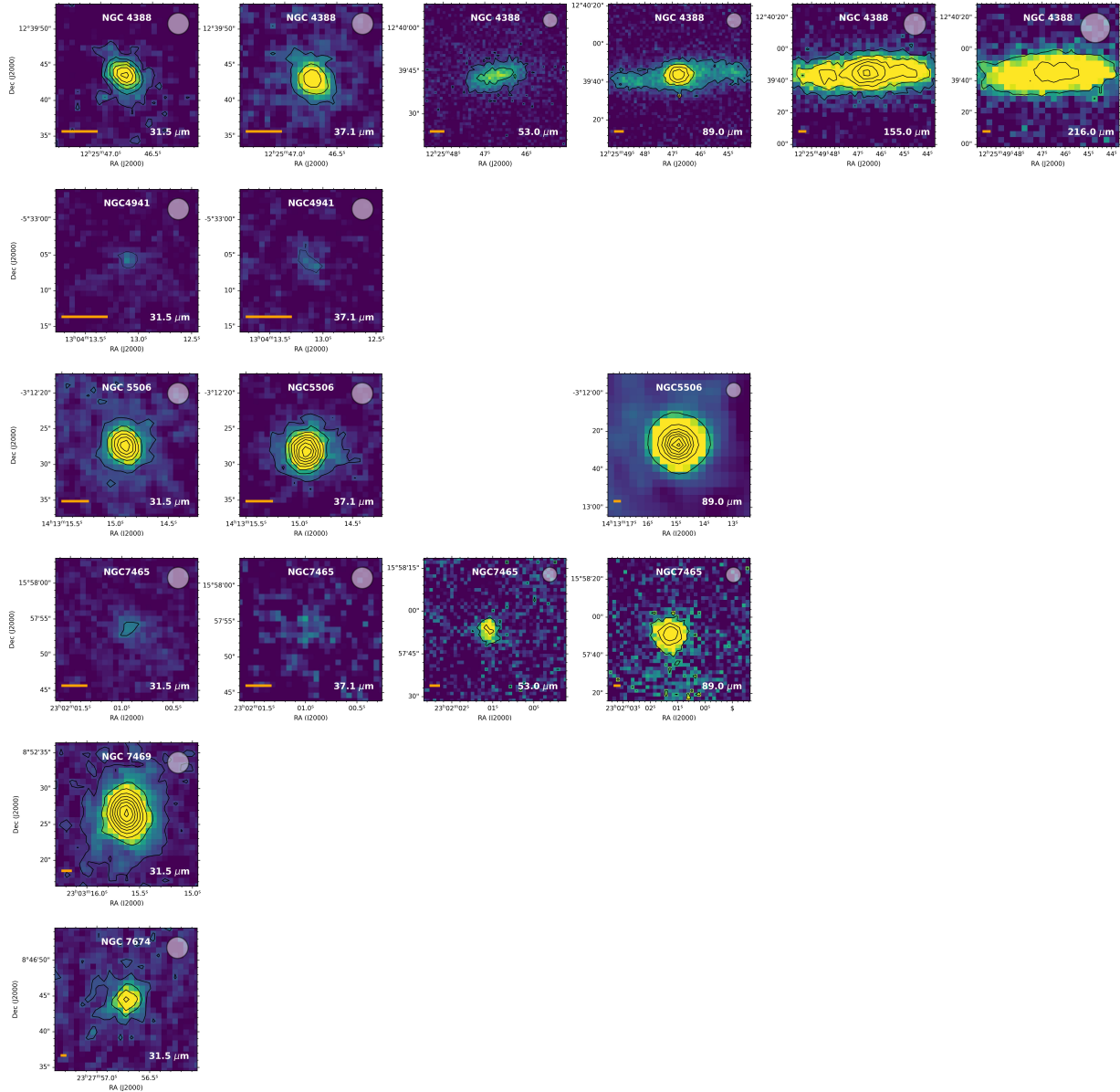


**Figure 5.** FORCAST 31.5 and 37.1  $\mu\text{m}$  images, and HAWC+ 53, 89, 155, and 215  $\mu\text{m}$  images. Each image has a differing FOV, which can be found in Table 3. The white transparent circle on the top right indicates the telescope beam size. The orange bar on the bottom left of the images is scaled to 500 pc. For all images, north is up and east is to the left.

emission at PA  $\sim 120^\circ$  at a  $3\sigma$  level at 37.1  $\mu\text{m}$ . Fuller et al. (2019) confirmed this elongation in the PSF-subtracted 37.1  $\mu\text{m}$  image coincident with the NLR and radio axes. Radomski et al. (2003) show extended emission in 10.8 and 18.2  $\mu\text{m}$  images that coincides with the NLR axis at PA  $\sim -60^\circ$ . For  $\geq 37.1 \mu\text{m}$ , we conclude that any extended emission due to NLR dust is within the FWHM of the SOFIA instruments.

**NGC 4258.** NGC 4258 was not detected but we include the data here since it is part of the sample. It has been observed and analyzed in the N-band with Gemini/Michelle by Mason et al. (2012). These authors found a compact nucleus that is marginally resolved at 10  $\mu\text{m}$  (FWHM  $\sim 0.5''$ ).

**NGC 4388.** NGC 4388 is an edge-on spiral that shows the most interesting mid- to far-IR morphology in this study. Notably, in the 30 - 40  $\mu\text{m}$  FORCAST images of NGC 4388, extension can be seen in the NE to SW direction at PA  $\sim 40^\circ$  (see also Fuller et al. 2019), coincident with the NLR. This emission is seen on smaller scales at shorter wavelengths (Asmus et al. 2016; García-Bernete et al. 2016). The 53  $\mu\text{m}$  image decreases in intensity and does not show a strong central core of emission as in the 31.5 – 37.1 wavelength range. However, at longer wavelengths (89 – 214  $\mu\text{m}$ ), host galaxy emission clearly dominates the images in the east-west direction at PA  $\sim 90^\circ$ .

**NGC 4941.** NGC 4941 is a low-luminosity AGN that appears here as a faint point-like source in the  $31.5\ \mu\text{m}$  and  $37.1\ \mu\text{m}$  images, but brighter at  $53$  and  $89\ \mu\text{m}$ . Subarcsecond resolution N-band imaging on VLT/VISIR (Asmus et al. 2011) showed no significant extended MIR sources outside of the nucleus.

**NGC 5506** NGC 5506 appears as a bright point source in both the  $31.5$  and  $37.1\ \mu\text{m}$  filters. While the nucleus is unresolved, extended MIR emission has been detected up to a few arcseconds to the northeast at  $11.9\ \mu\text{m}$  (Raban et al. 2008). Extended emission in the north-south direction was detected in the N-band out to  $\sim 560$  pc, while faint extended emission towards the east in the Q-band was also detected (García-Bernete et al. 2016). However, the PSF-subtracted  $12.27\ \mu\text{m}\ 2''\times 2''$  VLT/VISIR image of Alonso-Herrero et al. (2021) shows that the PA of extended emission varies from  $30^\circ$  in the central  $\sim 0.5''$  to nearly  $90^\circ$  in the outer regions.

**NGC 7465.** The  $31.5\ \mu\text{m}$  FORCAST image appears faint with a  $3\sigma$  upper-limit in the  $37.1\ \mu\text{m}$  image. The  $53$  and  $89\ \mu\text{m}$  HAWC+ images here appear increasingly brighter, albeit as point-like sources. Cold molecular gas observations (Young et al. 2021) reveal that NGC 7465 is quite gas-rich, possibly from a recent merger.

**NGC 7469.** NGC 7469 appears as a very bright source in the  $31.5\ \mu\text{m}$  image with  $\text{FWHM} \sim 4.3''$ . After PSF subtraction, Fuller et al. (2016) found extended emission in the north-south direction. This AGN is known to have a circumnuclear ring of star formation at a radius of  $\sim 480$  pc ( $\sim 1.4''$ ; Ramos Almeida et al. 2011) in  $8.7$  and  $18.3\ \mu\text{m}$  images taken on Gemini/T-ReCS. Recent JWST observations reveal prominent PAH emission, indicative of star formation, in the circumnuclear ring (García-Bernete et al. 2022b; Zhang & Ho 2023).

**NGC 7674.** The previously published (Fuller et al. 2016) FORCAST  $31.5\ \mu\text{m}$  image appears as a point-like source. Asmus et al. (2013) found that the nucleus of NGC 7674 is extended at  $\text{PA} \sim 125^\circ$  at subarcsecond scale resolution, where the extension roughly aligns with the ionization cone.

#### 4. NUCLEAR FLUX EXTRACTION

We aim to construct well-sampled mid- to far-IR SEDs of the nuclear emission of AGN at scales of several arcseconds, depending on the PSF of the observation and possible extended emission. On these scales, we expect multiple dust sources (i.e. torus, star forming regions, dusty outflow), however disentangling these sources is beyond the scope of this imaging atlas. Because the images span a range of observing cycles, instruments, and observing modes, we analyzed each image individually. Of our sample, 17 objects appear visually as point sources. For these sources, we performed aperture photometry where the aperture size was set to be  $2\times$  the FWHM at a given band. For objects that show host galaxy emission, we extract the central PSF to construct the SEDs as described below. We complement our SOFIA data with *Herschel* imaging data (see Appendix A) and use a similar analysis method to construct the full IR SEDs.

#### 4.1. Extended Sources: 2D Gaussian Fitting

For sources with extended dust emission, we performed a two-component simultaneous fit to accurately model both the central source based on the PSF, and the host galaxy whose fit assumes an elongated 2D Gaussian profile. In order to supplement the SOFIA data for the full mid- to far-IR SEDs, we used a similar methodology with *Herschel* images.

For the SOFIA images, the PSF used was based on the standard stars of the observing runs for each cycle as explained in Section 2.2. However, the same analysis could not be performed on *Herschel* images due to the threefold lobes associated with the instrument PSFs. To accommodate this, we compared three different PSF models to reproduce and fit the central source. Two of the PSFs were point source images while the third was an approximation of the theoretical instrumental PSF using a Gaussian profile. The fitting routine used four free parameters for the Gaussian profile: (1,2) the position in x and y of the PSF center according to the image center, (3) the amplitude of the PSF, (4) the fourth parameter was dependent on the PSF type used. For archival PSFs, this parameter represents the rotation angle that needs to be applied to the PSF to match the orientation of the image. For the Gaussian PSFs, this fourth parameter represents a scaling factor to the width of the Gaussian compared to its ideal value for a perfect instrument ( $1.22 \times \lambda/D$ ).

The galaxy background is defined by 7 parameters: (1,2) the 2D Gaussian's center position ( $x_0$  and  $y_0$ ), (3,4) its width ( $\sigma_x$  and  $\sigma_y$ ) in both directions, (5) its amplitude, and (6) its orientation on the image ( $\theta$ ). To these 6 parameters we added a constant background as a 7th free parameter. We combined these components and fit this simulated intensity map to the observed map using the 11 total free parameters (4 from the PSF and 7 from the 2D gaussian). We thus derived the parameters describing the best central source for our intensity maps, and then studied the properties extracted for the central source and removed it from the initial map to study the host galaxy itself. An example of this procedure is given in the Appendix in Figure 14.

#### 4.2. AGN and host galaxy contribution

While most SOFIA images were treated as point sources, Centaurus A, Circinus, NGC 1068, and NGC 4388 all had significant host galaxy contamination that needed to be subtracted from at least some of the images. Figure 6 shows the PSF subtracted images of these sources and Table 4 gives the percentage of the contribution of the PSF to the total flux of the object. In several other objects, the shorter wavelength ( $\sim 30 - 100\ \mu\text{m}$ ) images did not show host galaxy contamination, but longer wavelength *Herschel* images show the colder extended dust. Because this is an atlas of SOFIA images, we include objects with host galaxy contamination only in *Herschel* images in Appendix C for completeness.

The  $53\ \mu\text{m}$  image of Centaurus A contains ( $< 5\%$ ) emission from extended sources, so we performed aperture photometry to account for the central emission. At wavelengths  $\gtrsim 70\ \mu\text{m}$ , the host galaxy substantially ( $\sim 56 - 70\%$ ) contributes to the central AGN emission, so the extended emission was

subtracted. The PSF of Centaurus A at these wavelengths contributes  $\sim 35\%$ . This can be interpreted as the nucleus having a relatively constant IR contribution, so the brightness of the nucleus coincides with IR brightness of the host galaxy.

The PSF contribution of the Circinus Galaxy decreases between 53 and 160  $\mu\text{m}$  from 58 % to 35 %. At longer FIR wavelengths, the contribution of the PSF appears to be from the host galaxy and the fitting no longer provides information about the AGN. We interpret this as a decreasing IR contribution from the nucleus compared to the extended emission.

For the completeness of the SOFIA Atlas presented here, we used the 19-53  $\mu\text{m}$  images of NGC 1068 from Lopez-Rodriguez et al. (2018). These datasets were analyzed as described in that study and here we only present the results and images in that wavelength range. The study showed that the fractional contribution from star formation increases from 20 - 50  $\mu\text{m}$ , while extended emission from 200 K dust decreases. Emission from the torus peaks in this range, a result which is in agreement with Fuller et al. (2016) who found that the turnover in torus emission occurs at wavelengths  $\gtrsim 31.5 \mu\text{m}$ . Extended emission is observed here at all wavelengths  $\gtrsim 70 \mu\text{m}$  arising from dust in the host galaxy and star formation regions.

For NGC 4388, we show the results of PSF subtraction at all wavelengths, but only use the results in wavelengths  $\gtrsim 40 \mu\text{m}$  for the SED. In the 30 - 40  $\mu\text{m}$  range, the NE to SW extension is clear in the PSF-subtracted images. However, almost all of the extended emission lies within the FWHM of the observation; the FWHM of these images are only  $\sim 10\%$  greater than the FWHM of the PSF. Thus, while we show the PSF subtracted images of NGC 4388 here, for the SED we use the total 30 - 40  $\mu\text{m}$  fluxes which encompass the apparent extended emission due to the NLR. The change in the extended emission source and morphology between 40 and 70  $\mu\text{m}$  is clear in the PSF-subtracted images (Figure 6). The host galaxy clearly dominates the extended emission in the FIR while the NLR region dominates the extended emission in MIR wavelengths. The 53  $\mu\text{m}$  HAWC+ image appears to show the transition between dominant extended sources. The contribution of the PSF in the images of NGC 4388 is  $\sim 60\%$  in the 30 - 40  $\mu\text{m}$  range, where the extended emission is in the NE to SW direction. The contribution then decreases drastically to  $\sim 20\%$ . This reflects the turnover in extended emission seen in the images in Figure 5. The contribution of the PSF returns to  $\sim 70\%$  between 70 - 100  $\mu\text{m}$ , which suggests two separate but significant IR emission sources.

## 5. SPECTRAL ENERGY DISTRIBUTIONS

Tables 5 (SOFIA) and 6 (*Herschel*) give the nuclear fluxes of the AGN in our sample along with their associated errors in units of Jy. The sources of uncertainty here are the instrument calibration, sky background, and the 2D gaussian fitting, where applicable. We estimate FORCAST and HAWC+ errors at  $\sim 10\%$ . We use PACS instrument errors at 5%<sup>4</sup> and

SPIRE instrument errors as 5.5%<sup>5</sup>. The uncertainty due to sky background is determined on an individual basis, but averages  $\sim 5\%$ . The average uncertainty due to the 2-D gaussian fitting is  $\sim 1.5\%$ . We add these uncertainties in quadrature for the error bar estimation.

The nuclear SEDs are shown in Figure 7 in  $\nu F_\nu$ . The pink diamonds represent SOFIA observations while the black circles represent the complementary *Herschel* data. We obtained *Spitzer*/IRS spectra from the *Spitzer*/CASSIS database (Lebouteiller et al. 2011) for 21 of the 22 objects in our sample (solid black line). There was no spectrum available for NGC 7465. Low-resolution spectra ( $R \sim 100$ ) were obtained for 18 of the objects, while moderate resolution spectra ( $R \sim 600$ ) were available for Circinus, NGC 1068, and NGC 7674. This dataset provides the most completed SED coverage available between 30 - 500  $\mu\text{m}$ . Decomposing the SEDs in this sample is outside the scope of this manuscript, as we are presenting an imaging atlas. Here, we provide the main results and features of the SEDs of these objects.

The morphological changes seen in the extended emission source in Figure 5 for NGC 4388 are reflected in the SED at 53  $\mu\text{m}$ , where there is a marked decline in the SED. The drastic decrease seems to be due to the change of dominant emitting sources. The extended emission at wavelengths  $\lesssim 40 \mu\text{m}$  is due to dust in the direction of the radio axis, and the extended emission at wavelengths  $\gtrsim 50 \mu\text{m}$  is due to the host galaxy.

The wavelength of peak emission can give insight to the primary processes that drive MIR emission. The peak wavelength, determined by the highest flux from photometry and spectroscopy, ranges from 18 to 100  $\mu\text{m}$  in  $\nu F_\nu$  with an average of  $\sim 40 \mu\text{m}$ . This average only includes the peak in continuum values and does not take into account fine structure lines. Most (73%; 11 out of 15) Seyfert 2 have a peak emission at wavelengths  $\lesssim 40 \mu\text{m}$ . The SEDs of MCG-5-23-16, Mrk3, Mrk 573, NGC 1068, NGC 3081, and NGC 4151 peak at  $\sim 18$  - 20  $\mu\text{m}$ . This is in agreement with the correlation peak between the hard-X-rays and the mid-IR for Type 1 AGN in García-Bernete et al. (2017). The peak wavelengths in  $F_\nu$  (Jy) range  $\sim 20$  - 160  $\mu\text{m}$ , with an average  $\sim 93 \mu\text{m}$ . NGC 1068 is the only AGN to peak at the same wavelength in both sets of units.

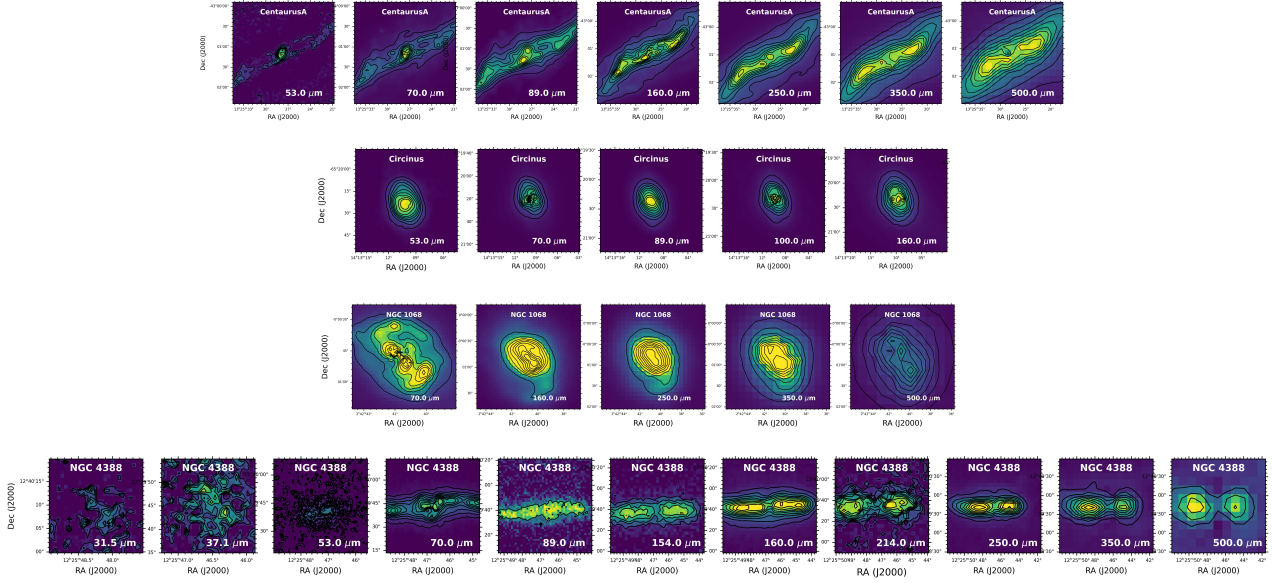
The *Spitzer* spectrum for NGC 1068 does not align with the SOFIA photometry because of the extensive PSF subtraction that we performed in the photometry that was not accounted for in the spectroscopy. This is the only object that not only has overlapping 20 - 40  $\mu\text{m}$  *Spitzer* and SOFIA data, but also that has had the background emission subtracted at these wavelengths.

### 5.1. Luminosity and Peak Wavelength

To test whether the peak wavelength is a function of luminosity, we plot  $L_{bol}$  vs  $\lambda_{peak}$ . Figure 8 shows the bolometric luminosities of the AGN plotted against the peak wavelength in the SEDs for both Sy1s, shown as red triangles, and Sy2s,

<sup>4</sup> PACS: <https://www.cosmos.esa.int/web/herschel/pacs-overview>

<sup>5</sup> SPIRE: <https://www.cosmos.esa.int/web/herschel/spire-overview>

**Figure 6.** PSF-subtracted images of host galaxy backgrounds**Table 4.** Contribution of the PSF to the host galaxy extended emission

Object	Wavelength ( $\mu\text{m}$ )												
	19.7	31.5	37.1	53	70	89	100	155	160	215	250	350	500
Centaurus A				...	30±1	34±1			31±1		36±2	37±2	44±2
Circinus				58±0.2	48±1	35±0.3	40±1		33±1				
NGC 1068	36±4	49±5	51±8	33±15	56±2				13±2		13 ± 1	35±1	54±1
NGC 4388	62±16	56±12	19±2	64±1	71±2			47±2	29±1	38±3	31±4	38±6	44±5

shown as purple stars. The correlation coefficient between the luminosity and peak wavelength is  $|R| \sim 0.63$  with statistical significance  $p = 0.0015$ . While it is argued that  $|R|$  of 0.6 - 0.7 may show moderate to strong correlation (see Section 3.2 in Messenger et al. 2013), a  $p$ -value  $\leq 0.05$  is generally accepted as statistically significant. The data suggests that higher luminosity objects have SEDs that peak at shorter wavelengths, which indicates the presence of a hot dust component in the vicinity of the AGN.

## 5.2. Mid- to Far-IR Colors

The ratio of  $F_{\nu}(70)/F_{\nu}(160)$  has been used as a proxy for dust temperature (Meléndez et al. 2014; García-González et al. 2016), where the ratio is higher for dust heated by the AGN and lower for dust heated by star formation. Here we perform this analysis using the ratio  $F_{\nu}(31)/F_{\nu}(70)$  by using the 31.5  $\mu\text{m}$  SOFIA data in our atlas. For objects that do not have data in the 31.5  $\mu\text{m}$  filter, we supplement that with data from the *Spitzer*/IRS continuum. NGC 7465 did not have 31.5  $\mu\text{m}$  flux data, nor did it have *Spitzer* data so we leave that object out of this analysis. Using the fluxes in Table 5, we plot a color-color diagram in  $F_{\nu}$  in Figure 9. This figure also visually shows the peak wavelength from the SEDs (in  $\nu F_{\nu}$ ).

Longer peak wavelengths tend to cluster at  $F_{\nu}(70)/F_{\nu}(160) \sim 1$  and  $F_{\nu}(31)/F_{\nu}(70) \sim 0.25 - 0.5$ .

In this sample we find an average  $F_{\nu}(70)/F_{\nu}(160)$  ratio of  $1.4 \pm 0.7$ . Previous studies (Meléndez et al. 2014; García-González et al. 2016) with larger sample sizes (313 and 33, respectively) have found an average ratio of  $\sim 0.8$ , albeit the data was analyzed using independent methods. This suggests a higher amount of AGN heated dust in our sample.

We find that 18 objects have  $F_{\nu}(31)/F_{\nu}(70) \gtrsim 1$ , with an average  $F_{\nu}(31)/F_{\nu}(70)$  of  $0.6 \pm 0.3$ . The only object with both  $F_{\nu}(70)/F_{\nu}(160)$  and  $F_{\nu}(31)/F_{\nu}(70) \gtrsim 1$  is MCG-5-23-16, and an SED that peaks  $\sim 20 \mu\text{m}$ . This object may be the most AGN dominated source in our sample. The other objects that show a peak at  $\sim 20 \mu\text{m}$  in  $\nu F_{\nu}$  still show  $F_{\nu}(31)/F_{\nu}(70) \gtrsim 1$ . Only one object, NGC 4388, shows  $F_{\nu}(31)/F_{\nu}(70) \gtrsim 1$  while  $F_{\nu}(70)/F_{\nu}(160) \gtrsim 1$ . This reflects the change in extended emission seen in Figure 5.

Half (11) of the objects in the sample show ratios  $F_{\nu}(31)/F_{\nu}(70) \gtrsim 1$  while  $F_{\nu}(70)/F_{\nu}(160) \gtrsim 1$ . These objects (Circinus, Mrk 231, Mrk 573, NGC 1275, NGC 2110, NGC 3081, NGC 3227, NGC 3281, NGC 4151, NGC 4941, NGC 5506, NGC 7469) are likely AGN dominated. Six objects show  $F_{\nu}(31)/F_{\nu}(70) \gtrsim 1$  and  $F_{\nu}(70)/F_{\nu}(160) \gtrsim 1$ , meaning that their SEDs peak at longer wavelengths. The emission from

**Table 5.** Nuclear fluxes for SOFIA/FORCAST and HAWC+ images.

Object	Wavelength ( $\mu\text{m}$ )						Ref
	31.5	37.1	53	89	155	215	
Centaurus A			10.7 $\pm$ 1.1	18.2 $\pm$ 2.1			This work
Circinus			85.8 $\pm$ 8.7	84.7 $\pm$ 8.52	51.5 $\pm$ 5.2		This work
MCG-5-23-16	1.8 $\pm$ 0.2		1.7 $\pm$ 0.2	0.7 $\pm$ 0.1	0.5 $\pm$ 0.1		a, This work
Mrk 3	2.9 $\pm$ 0.3	3.0 $\pm$ 0.3	3.1 $\pm$ 0.4	2.7 $\pm$ 0.3	2.1 $\pm$ 0.2		b, This work
Mrk 231				22.9 $\pm$ 2.3			This work
Mrk 573	0.7 $\pm$ 0.1	0.8 $\pm$ 0.1					b, This work
NGC 1068*	28.8 $\pm$ 1.8	29.7 $\pm$ 2.5	23.8 $\pm$ 4.8				c,d
NGC 1275	4.0 $\pm$ 0.4	5.0 $\pm$ 0.8		5.3 $\pm$ 0.2			b, This work
NGC 2110	1.3 $\pm$ 0.2		3.7 $\pm$ 0.5	4.4 $\pm$ 0.5	4.5 $\pm$ 0.5	2.2 $\pm$ 0.2	a, This work
NGC 2273	1.9 $\pm$ 0.2	2.7 $\pm$ 0.3	4.3 $\pm$ 0.5	6.5 $\pm$ 0.7	5.4 $\pm$ 0.6	3.8 $\pm$ 0.4	a, This work
NGC 2992	0.9 $\pm$ 0.1						a
NGC 3081	1.0 $\pm$ 0.1	1.4 $\pm$ 0.2					a,b
NGC 3227	2.3 $\pm$ 0.3	2.8 $\pm$ 0.3					a,b
NGC 3281	2.7 $\pm$ 0.3		5.3 $\pm$ 0.6	6.4 $\pm$ 0.7	4.6 $\pm$ 0.5	2.5 $\pm$ 0.3	a, This work
NGC 4151	3.9 $\pm$ 0.4	4.5 $\pm$ 0.3	4.9 $\pm$ 0.5	4.1 $\pm$ 0.4			b, This work
NGC 4258							This work
NGC 4388	3.0 $\pm$ 0.4	3.2 $\pm$ 0.3	0.7 $\pm$ 0.1	3.3 $\pm$ 0.4	3.4 $\pm$ 0.4	2.7 $\pm$ 0.3	a,b, This work
NGC 4941	0.29 $\pm$ 0.04	0.5 $\pm$ 0.1					This work
NGC 5506	4.1 $\pm$ 0.5	5.2 $\pm$ 0.5		7.0 $\pm$ 0.2			a, This work,e
NGC 7465			1.8 $\pm$ 0.2	4.9 $\pm$ 0.5			This work
NGC 7469	9.4 $\pm$ 1.1						a
NGC 7674	1.8 $\pm$ 0.2						a

REFERENCES: a) Fuller et al. (2016), b) Fuller et al. (2019), c) Lopez-Rodriguez et al. (2018), d) Lopez-Rodriguez et al. (2020), e) Lopez-Rodriguez et al. (2022b). \*Lopez-Rodriguez et al. (2018) measured the flux of NGC 1068 at 19.7  $\mu\text{m}$  to be 22.0  $\pm$  1.4.

these objects (Centaurus A, NGC 1068, NGC 2273, NGC 2992, NGC 4258, NGC 7674) are likely dominated by star formation.

## 6. CONCLUSIONS

We have presented a SOFIA atlas of nearby AGN in the 20 - 215  $\mu\text{m}$  wavelength range using FORCAST and HAWC+. We have released 69 observations of which 41 are newly published and 28 have been previously published (Fuller et al. 2016, 2019; Lopez-Rodriguez et al. 2018, 2022a). From these observations, NGC 4388 shows the most dramatic visual change in emission morphology. The 30 - 40  $\mu\text{m}$  images show a NE to SW dusty extension associated with the NLR, while the  $\gtrsim 50 \mu\text{m}$  images show a East to West dusty emission associated with the plane of the host galaxy. Our observations show that  $< 10''$  resolution 30 - 70  $\mu\text{m}$  observations are crucial to disentangle the emitting contribution from AGN and host galaxy.

We measured arcsecond scale unresolved nuclear fluxes in order to construct SEDs of the objects in our sample. We included complementary *Herschel* data to cover up to 500  $\mu\text{m}$ . For point sources we used aperture photometry to determine

the flux. For extended sources we used a 2D gaussian fitting method to extract the central unresolved source(s) of emission from the galaxy background. For this method, the PSF is scaled to represent the central emission while a 2D gaussian represents host galaxy or background emission. Based on the SEDs, we make the following conclusions:

- There is a sharp drop in the SED of NGC 4388 that corresponds to the wavelength where the angle of extended emission transitions from NE/SW (NLR) to E/W (host galaxy).
- The average peak of the SEDs is 40  $\mu\text{m}$  in  $\nu F_\nu$ , spanning a range of [20,100]  $\mu\text{m}$ .
- The peak wavelength of the SED appears to be a function of AGN luminosity, where higher luminosity objects peak at shorter wavelengths.
- MCG-5-23-16 is the only object whose color diagram shows both  $F_\nu(31)/F_\nu(70)$  and  $F_\nu(70)/F_\nu(160) \gtrsim 1$ , which may indicate an AGN dominated source.
- Half of the objects in the sample have flux ratios which suggest that the SED is dominated by AGN heated dust, while six objects show ratios consistent with heating by SF.

**Table 6.** Nuclear fluxes for *Herschel/PACS* and SPIRE images.

Object	Wavelength ( $\mu\text{m}$ )					
	70	100	160	250	350	500
Centaurus A	15.6 $\pm$ 1.0		19.9 $\pm$ 2.0	9.9 $\pm$ 1.0	6.9 $\pm$ 0.5	5.8 $\pm$ 0.4
Circinus	99.0 $\pm$ 5.3	63.5 $\pm$ 3.3	47.2 $\pm$ 2.4	20.1 $\pm$ 1.1	18.9 $\pm$ 1.2	6.5 $\pm$ 0.4
MCG-5-23-16	1.1 $\pm$ 0.1		0.34 $\pm$ 0.05	0.11 $\pm$ 0.02	0.05 $\pm$ 0.01	0.02 $\pm$ 0.005
Mrk 3	2.9 $\pm$ 0.2	2.6 $\pm$ 0.1	1.9 $\pm$ 0.1	0.9 $\pm$ 0.1	0.6 $\pm$ 0.1	0.34 $\pm$ 0.09
Mrk 231	31.2 $\pm$ 1.6	26.4 $\pm$ 1.4	13.9 $\pm$ 0.7	5.2 $\pm$ 0.3	1.8 $\pm$ 0.1	0.49 $\pm$ 0.03
Mrk 573	1.02 $\pm$ 0.05	1.05 $\pm$ 0.61	0.94 $\pm$ 0.06	0.44 $\pm$ 0.03	0.23 $\pm$ 0.02	0.08 $\pm$ 0.02
NGC 1068	101.7 $\pm$ 2.2		142.2 $\pm$ 0.5	69.7 $\pm$ 0.5	27.4 $\pm$ 0.4	8.8 $\pm$ 0.3
NGC 1275	6.8 $\pm$ 0.4	6.7 $\pm$ 0.4	5.5 $\pm$ 0.3	3.2 $\pm$ 0.2	2.7 $\pm$ 0.2	2.4 $\pm$ 0.1
NGC 2110	4.3 $\pm$ 0.2	5.0 $\pm$ 0.3	4.2 $\pm$ 0.2	1.7 $\pm$ 0.1	0.57 $\pm$ 0.09	0.20 $\pm$ 0.05
NGC 2273	5.2 $\pm$ 0.3	6.0 $\pm$ 0.3	5.8 $\pm$ 0.3	2.3 $\pm$ 0.1	0.93 $\pm$ 0.06	0.19 $\pm$ 0.02
NGC 2992	2.4 $\pm$ 0.1	3.3 $\pm$ 0.2	3.5 $\pm$ 0.2	1.9 $\pm$ 0.1	0.74 $\pm$ 0.04	0.54 $\pm$ 0.04
NGC 3081	1.9 $\pm$ 0.1	2.1 $\pm$ 0.1	1.6 $\pm$ 0.1	0.67 $\pm$ 0.04	0.24 $\pm$ 0.02	0.11 $\pm$ 0.02
NGC 3227	6.3 $\pm$ 0.3	8.3 $\pm$ 0.4	4.8 $\pm$ 0.3	2.1 $\pm$ 0.1	0.68 $\pm$ 0.04	0.16 $\pm$ 0.01
NGC 3281	6.4 $\pm$ 0.3	6.3 $\pm$ 0.3	4.5 $\pm$ 0.2	1.3 $\pm$ 0.1	0.38 $\pm$ 0.03	0.25 $\pm$ 0.03
NGC 4151	4.4 $\pm$ 0.2	3.1 $\pm$ 0.2	1.5 $\pm$ 0.1	0.40 $\pm$ 0.02	0.06 $\pm$ 0.005	0.0007 $\pm$ 7e $^{-5}$
NGC 4258	1.1 $\pm$ 0.2	4.1 $\pm$ 0.3	4.7 $\pm$ 0.5	3.3 $\pm$ 0.3	2.5 $\pm$ 0.3	0.9 $\pm$ 0.1
NGC 4388	2.9 $\pm$ 0.2		3.5 $\pm$ 0.2	1.1 $\pm$ 0.1	0.91 $\pm$ 0.08	0.49 $\pm$ 0.04
NGC 4941	0.80 $\pm$ 0.04		0.70 $\pm$ 0.08	0.12 $\pm$ 0.01	0.015 $\pm$ 0.001	0.05 $\pm$ 0.006
NGC 5506	6.8 $\pm$ 0.4	6.4 $\pm$ 0.3	3.9 $\pm$ 0.2	1.2 $\pm$ 0.1	0.53 $\pm$ 0.03	0.26 $\pm$ 0.03
NGC 7465	3.6 $\pm$ 0.2	4.9 $\pm$ 0.3	4.1 $\pm$ 0.2	1.8 $\pm$ 0.1	0.89 $\pm$ 0.07	0.42 $\pm$ 0.04
NGC 7469	22.8 $\pm$ 1.2	25.9 $\pm$ 1.3	18.3 $\pm$ 0.9	7.5 $\pm$ 0.4	2.9 $\pm$ 0.2	0.79 $\pm$ 0.05
NGC 7674	3.9 $\pm$ 0.2	4.5 $\pm$ 0.2	4.9 $\pm$ 0.3	2.7 $\pm$ 0.2	1.2 $\pm$ 0.1	0.44 $\pm$ 0.04

In future studies, we will combine data from this atlas with incoming data from JWST to update our IR datasets with the latest and highest resolution data available. Newly obtained JWST/MIRI observations will provide new higher angular resolution data for some of the sources in the wavelength range 5 - 28  $\mu\text{m}$ .

#### ACKNOWLEDGMENTS

We acknowledge Dr. Lucas Grosset for his effort in subtracting the image backgrounds. E.L.-R. is supported by the NASA/DLR Stratospheric Observatory for Infrared Astronomy (SOFIA) under the 08\_0012 Program. SOFIA is

jointly operated by the Universities Space Research Association, Inc. (USRA), under NASA contract NNA17BF53C, and the Deutsches SOFIA Institut (DSI) under DLR contract 50OK0901 to the University of Stuttgart. E.L.-R. is supported by the NASA Astrophysics Decadal Survey Precursor Science (ADSPS) Program (NNH22ZDA001N-ADSPS) with ID 22-ADSPS22-0009 and agreement number 80NSSC23K1585. I.G.B. acknowledges support from STFC through grants ST/S000488/1 and ST/W000903/1. C.R. acknowledges support from Fondecyt Regular grant 1230345 and ANID BASAL project FB210003.

*Software:* ASTROPY (Astropy Collaboration et al. 2022, 2018, 2013); SciPy Virtanen et al. (2020)

#### REFERENCES

- Alonso-Herrero, A., Ramos Almeida, C., Mason, R., et al. 2011, ApJ, 736, 82, doi: [10.1088/0004-637X/736/2/82](https://doi.org/10.1088/0004-637X/736/2/82)
- Alonso-Herrero, A., Ramos Almeida, C., Esquej, P., et al. 2014, MNRAS, 443, 2766, doi: [10.1093/mnras/stu1293](https://doi.org/10.1093/mnras/stu1293)
- Alonso-Herrero, A., Esquej, P., Roche, P. F., et al. 2016, MNRAS, 455, 563, doi: [10.1093/mnras/stv2342](https://doi.org/10.1093/mnras/stv2342)
- Alonso-Herrero, A., Pereira-Santaella, M., García-Burillo, S., et al. 2018, ApJ, 859, 144, doi: [10.3847/1538-4357/aabe30](https://doi.org/10.3847/1538-4357/aabe30)
- Alonso-Herrero, A., García-Burillo, S., Hönig, S. F., et al. 2021, A&A, 652, A99, doi: [10.1051/0004-6361/202141219](https://doi.org/10.1051/0004-6361/202141219)
- Antonucci, R. 1993, ARA&A, 31, 473, doi: [10.1146/annurev.aa.31.090193.002353](https://doi.org/10.1146/annurev.aa.31.090193.002353)

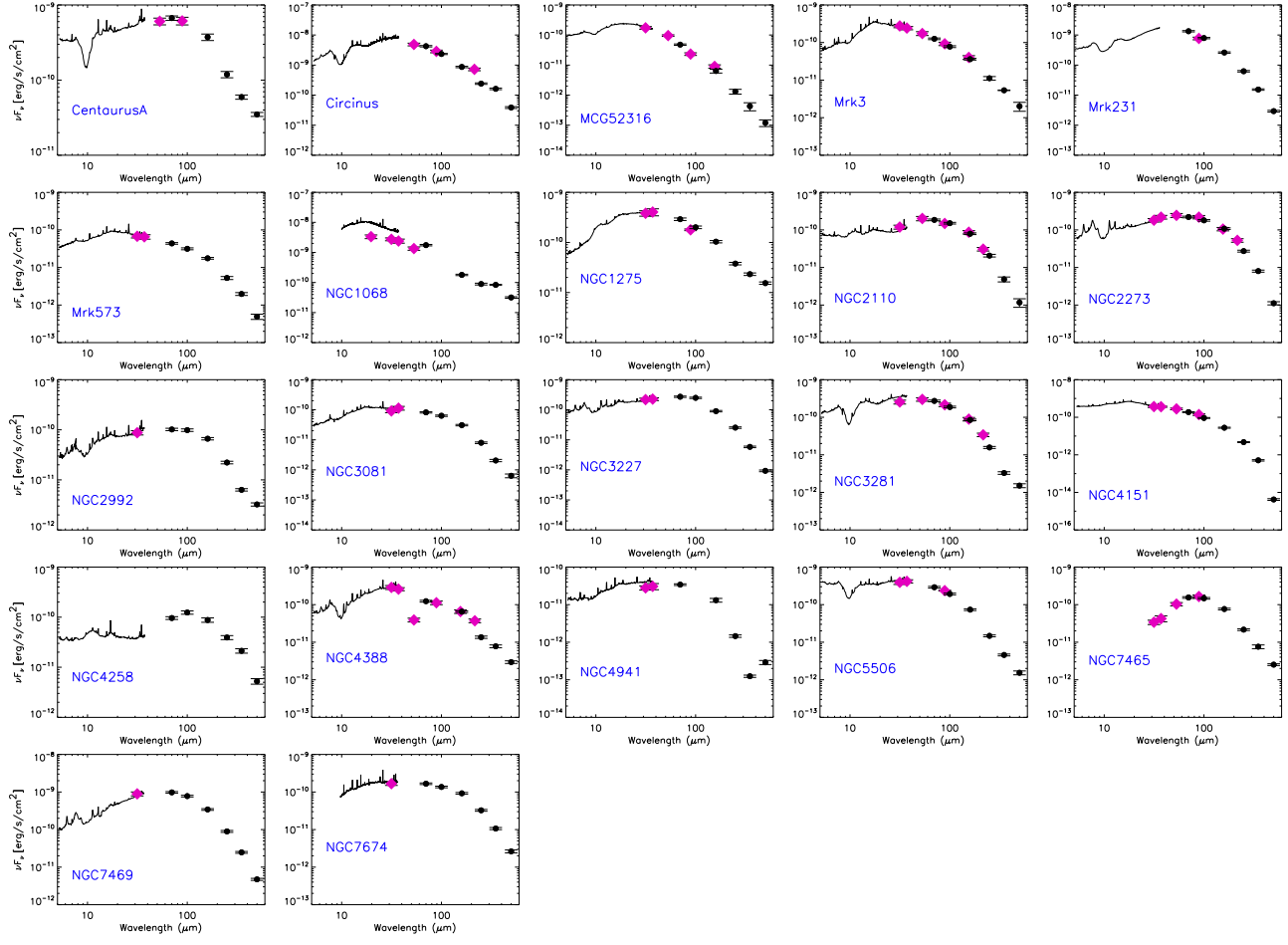


**Figure 7.** Mid-to-far-IR SEDs of the several-arcsecond-scale nuclear fluxes in our sample of AGN. Pink diamonds represent SOFIA observations while black dots represent complementary Herschel observations. The solid black lines correspond to *Spitzer* spectra.

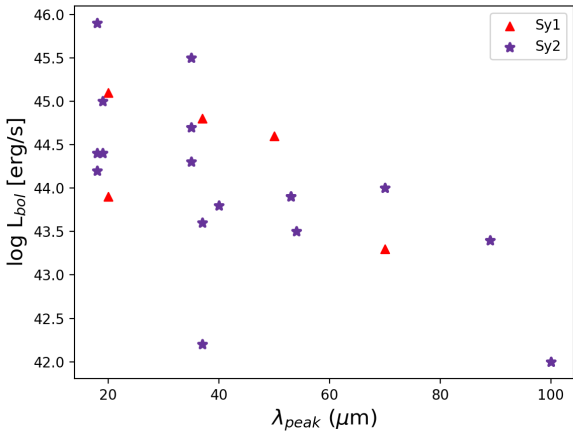


**Figure 8.** Bolometric luminosity vs the peak wavelength of the SED for both Sy1 (red triangles) and Sy2 (purple stars).

Antonucci, R. R. J., & Miller, J. S. 1985, ApJ, 297, 621,

doi: 10.1086/163559

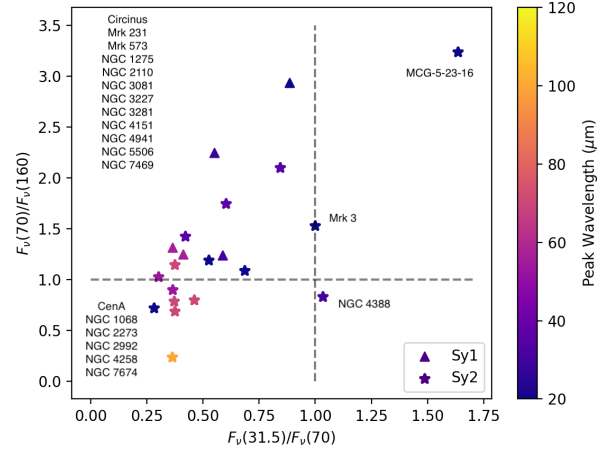


**Figure 9.** Color diagram of 21 of the 22 AGN in our sample. Sy 1 are represented by triangles while Sy 2 are stars. The scale on the right shows peak wavelength by color.

Asmus, D. 2019, MNRAS, 489, 2177, doi: 10.1093/mnras/stz2289

- Asmus, D., Gandhi, P., Smette, A., Höning, S. F., & Duschl, W. J. 2011, A&A, 536, A36, doi: [10.1051/0004-6361/201116693](https://doi.org/10.1051/0004-6361/201116693)
- Asmus, D., Hoenig, S., Gandhi, P., Smette, A., & Duschl, W. 2013, Sasmirala Subarcsecond mid-infrared atlas of local AGN, VO resource provided by the GAVO Data Center.  
<http://dc.zah.uni-heidelberg.de/sasmirala/q/im/info>
- Asmus, D., Höning, S. F., & Gandhi, P. 2016, ApJ, 822, 109, doi: [10.3847/0004-637X/822/2/109](https://doi.org/10.3847/0004-637X/822/2/109)
- Asmus, D., Höning, S. F., Gandhi, P., Smette, A., & Duschl, W. J. 2014, MNRAS, 439, 1648, doi: [10.1093/mnras/stu041](https://doi.org/10.1093/mnras/stu041)
- Astropy Collaboration, Robitaille, T. P., Tollerud, E. J., et al. 2013, A&A, 558, A33, doi: [10.1051/0004-6361/201322068](https://doi.org/10.1051/0004-6361/201322068)
- Astropy Collaboration, Price-Whelan, A. M., Sipőcz, B. M., et al. 2018, AJ, 156, 123, doi: [10.3847/1538-3881/aabc4f](https://doi.org/10.3847/1538-3881/aabc4f)
- Astropy Collaboration, Price-Whelan, A. M., Lim, P. L., et al. 2022, apj, 935, 167, doi: [10.3847/1538-4357/ac7c74](https://doi.org/10.3847/1538-4357/ac7c74)
- Baumgartner, W. H., Tueller, J., Markwardt, C. B., et al. 2013, ApJS, 207, 19, doi: [10.1088/0067-0049/207/2/19](https://doi.org/10.1088/0067-0049/207/2/19)
- Bock, J. J., Neugebauer, G., Matthews, K., et al. 2000, AJ, 120, 2904, doi: [10.1086/316871](https://doi.org/10.1086/316871)
- Borkar, A., Adhikari, T. P., Różańska, A., et al. 2021, MNRAS, 500, 3536, doi: [10.1093/mnras/staa3515](https://doi.org/10.1093/mnras/staa3515)
- Burtscher, L., Meisenheimer, K., Tristram, K. R. W., et al. 2013, A&A, 558, A149, doi: [10.1051/0004-6361/201321890](https://doi.org/10.1051/0004-6361/201321890)
- Buta, R. 1990, ApJ, 351, 62, doi: [10.1086/168444](https://doi.org/10.1086/168444)
- Buta, R., Alpert, A. J., Cobb, M. L., Crocker, D. A., & Purcell, G. B. 1998, AJ, 116, 1142, doi: [10.1086/300494](https://doi.org/10.1086/300494)
- Buta, R. J., Byrd, G. G., & Freeman, T. 2004, AJ, 127, 1982, doi: [10.1086/382239](https://doi.org/10.1086/382239)
- Capetti, A., Macchettò, F., Axon, D., Sparks, W., & Boksenberg, A. 1995, ApJ, 448, 600, doi: [10.1086/175989](https://doi.org/10.1086/175989)
- Conselice, C. J., Gallagher, John S., I., & Wyse, R. F. G. 2001, AJ, 122, 2281, doi: [10.1086/323534](https://doi.org/10.1086/323534)
- Davies, R. I., Thomas, J., Genzel, R., et al. 2006, ApJ, 646, 754, doi: [10.1086/504963](https://doi.org/10.1086/504963)
- Duras, F., Bongiorno, A., Ricci, F., et al. 2020, A&A, 636, A73, doi: [10.1051/0004-6361/201936817](https://doi.org/10.1051/0004-6361/201936817)
- Emmering, R. T., Blandford, R. D., & Shlosman, I. 1992, ApJ, 385, 460, doi: [10.1086/170955](https://doi.org/10.1086/170955)
- Fabian, A. C., Johnstone, R. M., Sanders, J. S., et al. 2008, Nature, 454, 968, doi: [10.1038/nature07169](https://doi.org/10.1038/nature07169)
- Ferruit, P., Wilson, A. S., & Mulchaey, J. 2000, ApJS, 128, 139, doi: [10.1086/313379](https://doi.org/10.1086/313379)
- Fuller, L., Lopez-Rodríguez, E., Packham, C., et al. 2016, MNRAS, 462, 2618, doi: [10.1093/mnras/stw1780](https://doi.org/10.1093/mnras/stw1780)
- . 2019, MNRAS, 483, 3404, doi: [10.1093/mnras/sty3338](https://doi.org/10.1093/mnras/sty3338)
- Gámez Rosas, V., Isbell, J. W., Jaffe, W., et al. 2022, Nature, 602, 403, doi: [10.1038/s41586-021-04311-7](https://doi.org/10.1038/s41586-021-04311-7)
- García-Bernete, I., Ramos Almeida, C., Landt, H., et al. 2017, MNRAS, 469, 110, doi: [10.1093/mnras/stx795](https://doi.org/10.1093/mnras/stx795)
- García-Bernete, I., Ramos Almeida, C., Acosta-Pulido, J. A., et al. 2015, MNRAS, 449, 1309, doi: [10.1093/mnras/stv338](https://doi.org/10.1093/mnras/stv338)
- García-Bernete, I., Ramos Almeida, C., Acosta-Pulido, J. A., et al. 2016, MNRAS, 463, 3531, doi: [10.1093/mnras/stw2125](https://doi.org/10.1093/mnras/stw2125)
- García-Bernete, I., González-Martín, O., Ramos Almeida, C., et al. 2022a, A&A, 667, A140, doi: [10.1051/0004-6361/202244230](https://doi.org/10.1051/0004-6361/202244230)
- García-Bernete, I., Rigopoulou, D., Alonso-Herrero, A., et al. 2022b, A&A, 666, L5, doi: [10.1051/0004-6361/202244806](https://doi.org/10.1051/0004-6361/202244806)
- García-Bernete, I., Alonso-Herrero, A., Rigopoulou, D., et al. 2024, A&A, 681, L7, doi: [10.1051/0004-6361/202348266](https://doi.org/10.1051/0004-6361/202348266)
- García-Burillo, S., Combes, F., Ramos Almeida, C., et al. 2016, ApJL, 823, L12, doi: [10.3847/2041-8205/823/1/L12](https://doi.org/10.3847/2041-8205/823/1/L12)
- García-Burillo, S., Combes, F., Ramos Almeida, C., et al. 2019, A&A, 632, A61, doi: [10.1051/0004-6361/201936606](https://doi.org/10.1051/0004-6361/201936606)
- García-Burillo, S., Alonso-Herrero, A., Ramos Almeida, C., et al. 2021, A&A, 652, A98, doi: [10.1051/0004-6361/202141075](https://doi.org/10.1051/0004-6361/202141075)
- García-González, J., Alonso-Herrero, A., Hernán-Caballero, A., et al. 2016, MNRAS, 458, 4512, doi: [10.1093/mnras/stw626](https://doi.org/10.1093/mnras/stw626)
- González-Martín, O., Rodríguez-Espinosa, J. M., Díaz-Santos, T., et al. 2013, A&A, 553, A35, doi: [10.1051/0004-6361/201220382](https://doi.org/10.1051/0004-6361/201220382)
- Haidar, H., Rosario, D. J., Alonso-Herrero, A., et al. 2024, arXiv e-prints, arXiv:2404.16100, doi: [10.48550/arXiv.2404.16100](https://doi.org/10.48550/arXiv.2404.16100)
- Harris, G. L. H., Rejkuba, M., & Harris, W. E. 2010, PASA, 27, 457, doi: [10.1071/AS09061](https://doi.org/10.1071/AS09061)
- Hatziminaoglou, E., Hernán-Caballero, A., Feltre, A., & Piñol Ferrer, N. 2015, ApJ, 803, 110, doi: [10.1088/0004-637X/803/2/110](https://doi.org/10.1088/0004-637X/803/2/110)
- Herter, T. L., Adams, J. D., De Buizer, J. M., et al. 2012, ApJL, 749, L18, doi: [10.1088/2041-8205/749/2/L18](https://doi.org/10.1088/2041-8205/749/2/L18)
- Holtzman, J. A., Faber, S. M., Shaya, E. J., et al. 1992, AJ, 103, 691, doi: [10.1086/116094](https://doi.org/10.1086/116094)
- Höning, S. F. 2019, ApJ, 884, 171, doi: [10.3847/1538-4357/ab4591](https://doi.org/10.3847/1538-4357/ab4591)
- Höning, S. F., Kishimoto, M., Antonucci, R., et al. 2012, ApJ, 755, 149, doi: [10.1088/0004-637X/755/2/149](https://doi.org/10.1088/0004-637X/755/2/149)
- Ichikawa, K., Ricci, C., Ueda, Y., et al. 2017, ApJ, 835, 74, doi: [10.3847/1538-4357/835/1/74](https://doi.org/10.3847/1538-4357/835/1/74)
- Imanishi, M., Nakanishi, K., Izumi, T., & Wada, K. 2018, ApJL, 853, L25, doi: [10.3847/2041-8213/aaa8df](https://doi.org/10.3847/2041-8213/aaa8df)
- Imanishi, M., Nguyen, D. D., Wada, K., et al. 2020, ApJ, 902, 99, doi: [10.3847/1538-4357/abaf50](https://doi.org/10.3847/1538-4357/abaf50)
- Isbell, J. W., Meisenheimer, K., Pott, J. U., et al. 2022, A&A, 663, A35, doi: [10.1051/0004-6361/202243271](https://doi.org/10.1051/0004-6361/202243271)
- Kakkad, D., Stalevski, M., Kishimoto, M., et al. 2023, MNRAS, 519, 5324, doi: [10.1093/mnras/stac3827](https://doi.org/10.1093/mnras/stac3827)
- Kovács, A. 2008, in Society of Photo-Optical Instrumentation Engineers (SPIE) Conference Series, Vol. 7020, Millimeter and Submillimeter Detectors and Instrumentation for Astronomy IV, ed. W. D. Duncan, W. S. Holland, S. Withington, & J. Zmuidzinas, 70201S, doi: [10.1117/12.790276](https://doi.org/10.1117/12.790276)

- Kovács, A., Chapman, S. C., Dowell, C. D., et al. 2006, *ApJ*, 650, 592, doi: [10.1086/506341](https://doi.org/10.1086/506341)
- Kukula, M. J., Ghosh, T., Pedlar, A., et al. 1993, *MNRAS*, 264, 893, doi: [10.1093/mnras/264.4.893](https://doi.org/10.1093/mnras/264.4.893)
- Lebouteiller, V., Barry, D. J., Spoon, H. W. W., et al. 2011, *ApJS*, 196, 8, doi: [10.1088/0067-0049/196/1/8](https://doi.org/10.1088/0067-0049/196/1/8)
- Leighly, K. M., Terndrup, D. M., Baron, E., et al. 2014, *ApJ*, 788, 123, doi: [10.1088/0004-637X/788/2/123](https://doi.org/10.1088/0004-637X/788/2/123)
- López-Gonzaga, N., Burtscher, L., Tristram, K. R. W., Meisenheimer, K., & Schartmann, M. 2016, *A&A*, 591, A47, doi: [10.1051/0004-6361/201527590](https://doi.org/10.1051/0004-6361/201527590)
- López-Gonzaga, N., Jaffe, W., Burtscher, L., Tristram, K. R. W., & Meisenheimer, K. 2014, *A&A*, 565, A71, doi: [10.1051/0004-6361/201323002](https://doi.org/10.1051/0004-6361/201323002)
- Lopez-Rodriguez, E. 2021, *Nature Astronomy*, 5, 604, doi: [10.1038/s41550-021-01329-9](https://doi.org/10.1038/s41550-021-01329-9)
- Lopez-Rodriguez, E., Kishimoto, M., Antonucci, R., et al. 2022a, arXiv e-prints, arXiv:2207.09466. <https://arxiv.org/abs/2207.09466>
- . 2023, *ApJ*, 951, 31, doi: [10.3847/1538-4357/accb96](https://doi.org/10.3847/1538-4357/accb96)
- Lopez-Rodriguez, E., Packham, C., Jones, T. J., et al. 2015, *MNRAS*, 452, 1902, doi: [10.1093/mnras/stv1410](https://doi.org/10.1093/mnras/stv1410)
- Lopez-Rodriguez, E., Fuller, L., Alonso-Herrero, A., et al. 2018, ArXiv e-prints. <https://arxiv.org/abs/1804.04134>
- Lopez-Rodriguez, E., Dowell, C. D., Jones, T. J., et al. 2020, *ApJ*, 888, 66, doi: [10.3847/1538-4357/ab5849](https://doi.org/10.3847/1538-4357/ab5849)
- Lopez-Rodriguez, E., Clarke, M., Shenoy, S., et al. 2022b, *ApJ*, 936, 65, doi: [10.3847/1538-4357/ac83ac](https://doi.org/10.3847/1538-4357/ac83ac)
- Marconi, A., Risaliti, G., Gilli, R., et al. 2004, *MNRAS*, 351, 169, doi: [10.1111/j.1365-2966.2004.07765.x](https://doi.org/10.1111/j.1365-2966.2004.07765.x)
- Marinucci, A., Bianchi, S., Nicastro, F., Matt, G., & Goulding, A. D. 2012, *ApJ*, 748, 130, doi: [10.1088/0004-637X/748/2/130](https://doi.org/10.1088/0004-637X/748/2/130)
- Martini, P., Regan, M. W., Mulchaey, J. S., & Pogge, R. W. 2003, *ApJS*, 146, 353, doi: [10.1086/367817](https://doi.org/10.1086/367817)
- Mason, R. E., Geballe, T. R., Packham, C., et al. 2006, *ApJ*, 640, 612, doi: [10.1086/500299](https://doi.org/10.1086/500299)
- Mason, R. E., Levenson, N. A., Shi, Y., et al. 2009, *ApJL*, 693, L136, doi: [10.1088/0004-637X/693/2/L136](https://doi.org/10.1088/0004-637X/693/2/L136)
- Mason, R. E., Lopez-Rodriguez, E., Packham, C., et al. 2012, *AJ*, 144, 11, doi: [10.1088/0004-6256/144/1/11](https://doi.org/10.1088/0004-6256/144/1/11)
- Meléndez, M., Mushotzky, R. F., Shimizu, T. T., Barger, A. J., & Cowie, L. L. 2014, *ApJ*, 794, 152, doi: [10.1088/0004-637X/794/2/152](https://doi.org/10.1088/0004-637X/794/2/152)
- Messenger, S. J., Speck, A., & Volk, K. 2013, *ApJ*, 764, 142, doi: [10.1088/0004-637X/764/2/142](https://doi.org/10.1088/0004-637X/764/2/142)
- Mor, R., & Netzer, H. 2012, *MNRAS*, 420, 526, doi: [10.1111/j.1365-2966.2011.20060.x](https://doi.org/10.1111/j.1365-2966.2011.20060.x)
- Mor, R., Netzer, H., & Elitzur, M. 2009, *ApJ*, 705, 298, doi: [10.1088/0004-637X/705/1/298](https://doi.org/10.1088/0004-637X/705/1/298)
- Mulchaey, J. S., Wilson, A. S., Bower, G. A., et al. 1994, *ApJ*, 433, 625, doi: [10.1086/174671](https://doi.org/10.1086/174671)
- Nenkova, M., Sirocky, M. M., Ivezić, Ž., & Elitzur, M. 2008a, *ApJ*, 685, 147, doi: [10.1086/590482](https://doi.org/10.1086/590482)
- Nenkova, M., Sirocky, M. M., Nikutta, R., Ivezić, Ž., & Elitzur, M. 2008b, *ApJ*, 685, 160, doi: [10.1086/590483](https://doi.org/10.1086/590483)
- Packham, C., Radomski, J. T., Roche, P. F., et al. 2005, *ApJL*, 618, L17, doi: [10.1086/427691](https://doi.org/10.1086/427691)
- Pogge, R. W., & De Robertis, M. M. 1995, *ApJ*, 451, 585, doi: [10.1086/176246](https://doi.org/10.1086/176246)
- Quillen, A. C., Brookes, M. H., Keene, J., et al. 2006, *ApJ*, 645, 1092, doi: [10.1086/504418](https://doi.org/10.1086/504418)
- Raban, D., Heijligers, B., Röttgering, H., et al. 2008, *A&A*, 484, 341, doi: [10.1051/0004-6361:20077444](https://doi.org/10.1051/0004-6361:20077444)
- Radomski, J. T., Piña, R. K., Packham, C., et al. 2003, *ApJ*, 587, 117, doi: [10.1086/367612](https://doi.org/10.1086/367612)
- Radomski, J. T., Packham, C., Levenson, N. A., et al. 2008, *ApJ*, 681, 141, doi: [10.1086/587771](https://doi.org/10.1086/587771)
- Ramos Almeida, C., & Ricci, C. 2017, *Nature Astronomy*, 1, 679, doi: [10.1038/s41550-017-0232-z](https://doi.org/10.1038/s41550-017-0232-z)
- Ramos Almeida, C., Levenson, N. A., Rodríguez Espinosa, J. M., et al. 2009, *ApJ*, 702, 1127, doi: [10.1088/0004-637X/702/2/1127](https://doi.org/10.1088/0004-637X/702/2/1127)
- Ramos Almeida, C., Levenson, N. A., Alonso-Herrero, A., et al. 2011, *ApJ*, 731, 92, doi: [10.1088/0004-637X/731/2/92](https://doi.org/10.1088/0004-637X/731/2/92)
- Rupke, D. S., Veilleux, S., & Sanders, D. B. 2005, *ApJ*, 632, 751, doi: [10.1086/444451](https://doi.org/10.1086/444451)
- Rupke, D. S. N., & Veilleux, S. 2011, *ApJL*, 729, L27, doi: [10.1088/2041-8205/729/2/L27](https://doi.org/10.1088/2041-8205/729/2/L27)
- Sani, E., Davies, R. I., Sternberg, A., et al. 2012, *MNRAS*, 424, 1963, doi: [10.1111/j.1365-2966.2012.21333.x](https://doi.org/10.1111/j.1365-2966.2012.21333.x)
- Schinnerer, E., Eckart, A., & Tacconi, L. J. 2001, *ApJ*, 549, 254, doi: [10.1086/319052](https://doi.org/10.1086/319052)
- Stalevski, M., Asmus, D., & Tristram, K. R. W. 2017, *MNRAS*, 472, 3854, doi: [10.1093/mnras/stx2227](https://doi.org/10.1093/mnras/stx2227)
- Stalevski, M., González-Gaitán, S., Savić, D., et al. 2023, *MNRAS*, 519, 3237, doi: [10.1093/mnras/stac3753](https://doi.org/10.1093/mnras/stac3753)
- Stalevski, M., Tristram, K. R. W., & Asmus, D. 2019, *MNRAS*, 484, 3334, doi: [10.1093/mnras/stz220](https://doi.org/10.1093/mnras/stz220)
- Takasao, S., Shuto, Y., & Wada, K. 2022, *ApJ*, 926, 50, doi: [10.3847/1538-4357/ac38a8](https://doi.org/10.3847/1538-4357/ac38a8)
- Tristram, K. R. W., Burtscher, L., Jaffe, W., et al. 2014, *A&A*, 563, A82, doi: [10.1051/0004-6361/201322698](https://doi.org/10.1051/0004-6361/201322698)
- Tully, R. B., Rizzi, L., Shaya, E. J., et al. 2009, *AJ*, 138, 323, doi: [10.1088/0004-6256/138/2/323](https://doi.org/10.1088/0004-6256/138/2/323)
- Ulvestad, J. S., & Wilson, A. S. 1984, *ApJ*, 278, 544, doi: [10.1086/161821](https://doi.org/10.1086/161821)
- Urry, C. M., & Padovani, P. 1995, *PASP*, 107, 803, doi: [10.1086/133630](https://doi.org/10.1086/133630)
- Venanzo, M., Höning, S., & Williamson, D. 2020, *ApJ*, 900, 174, doi: [10.3847/1538-4357/aba89f](https://doi.org/10.3847/1538-4357/aba89f)

- Virtanen, P., Gommers, R., Oliphant, T. E., et al. 2020, Nature Methods, 17, 261, doi: [10.1038/s41592-019-0686-2](https://doi.org/10.1038/s41592-019-0686-2)
- Young, L. M., Meier, D. S., Bureau, M., et al. 2021, ApJ, 909, 98, doi: [10.3847/1538-4357/abe126](https://doi.org/10.3847/1538-4357/abe126)
- Yuan, F., Markoff, S., Falcke, H., & Biermann, P. L. 2002, A&A, 391, 139, doi: [10.1051/0004-6361:20020817](https://doi.org/10.1051/0004-6361:20020817)
- Zhang, L., & Ho, L. C. 2023, ApJL, 953, L9, doi: [10.3847/2041-8213/acea73](https://doi.org/10.3847/2041-8213/acea73)

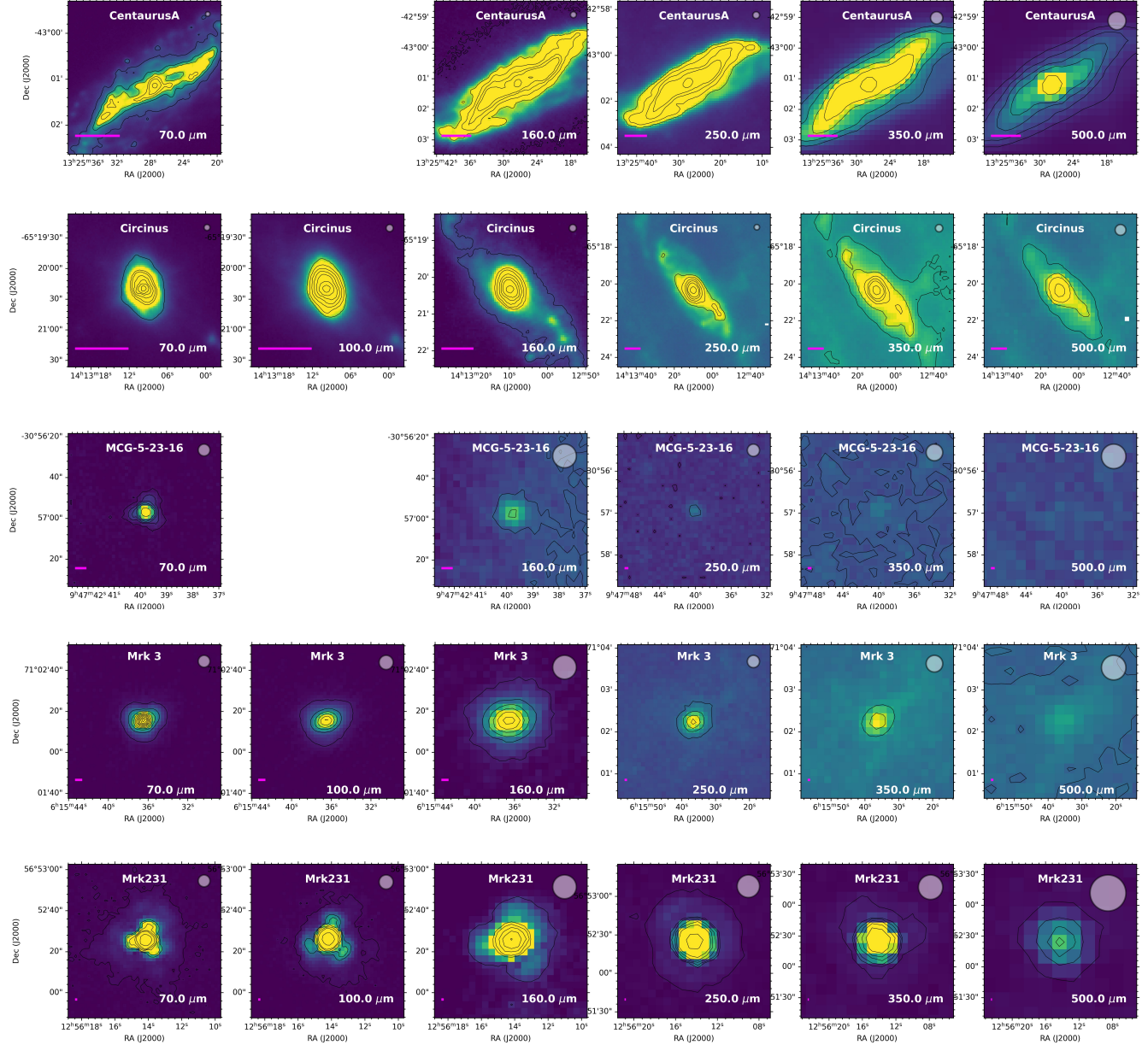


**Figure 10.** *Herschel* PACS and SPIRE FIR images. The white circle in the top right indicates the beam size of the observation, while the pink line in the bottom left indicates a distance of 1 kpc.

## APPENDIX

### A. HERSCHEL IMAGES

We used images from the *Herschel* Archive to supplement SOFIA data in FIR wavelengths. Images from the PACS and SPIRE instruments covering the wavelength range 70 - 500  $\mu\text{m}$  are shown in Figures 10, 11, 12, and 13. The white circle in the upper right indicates the beam size while the pink scale in the bottom left indicates a distance of 1 kpc. To extract nuclear fluxes on scales of several arcseconds, we use the methods described in Section 4. For point sources, we performed aperture photometry. For extended sources, we used the 2D gaussian routine outlined in Section 4.1.

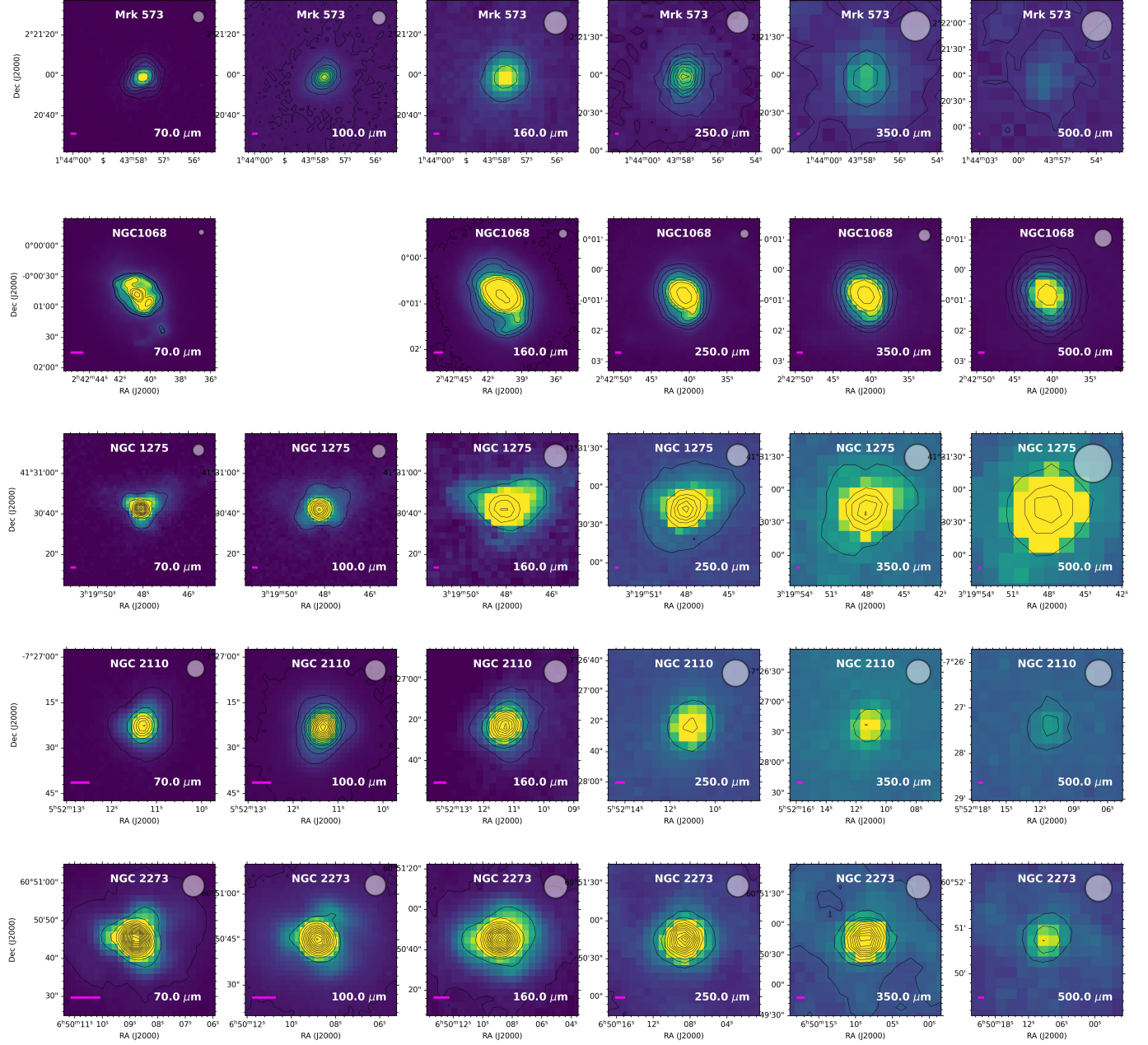


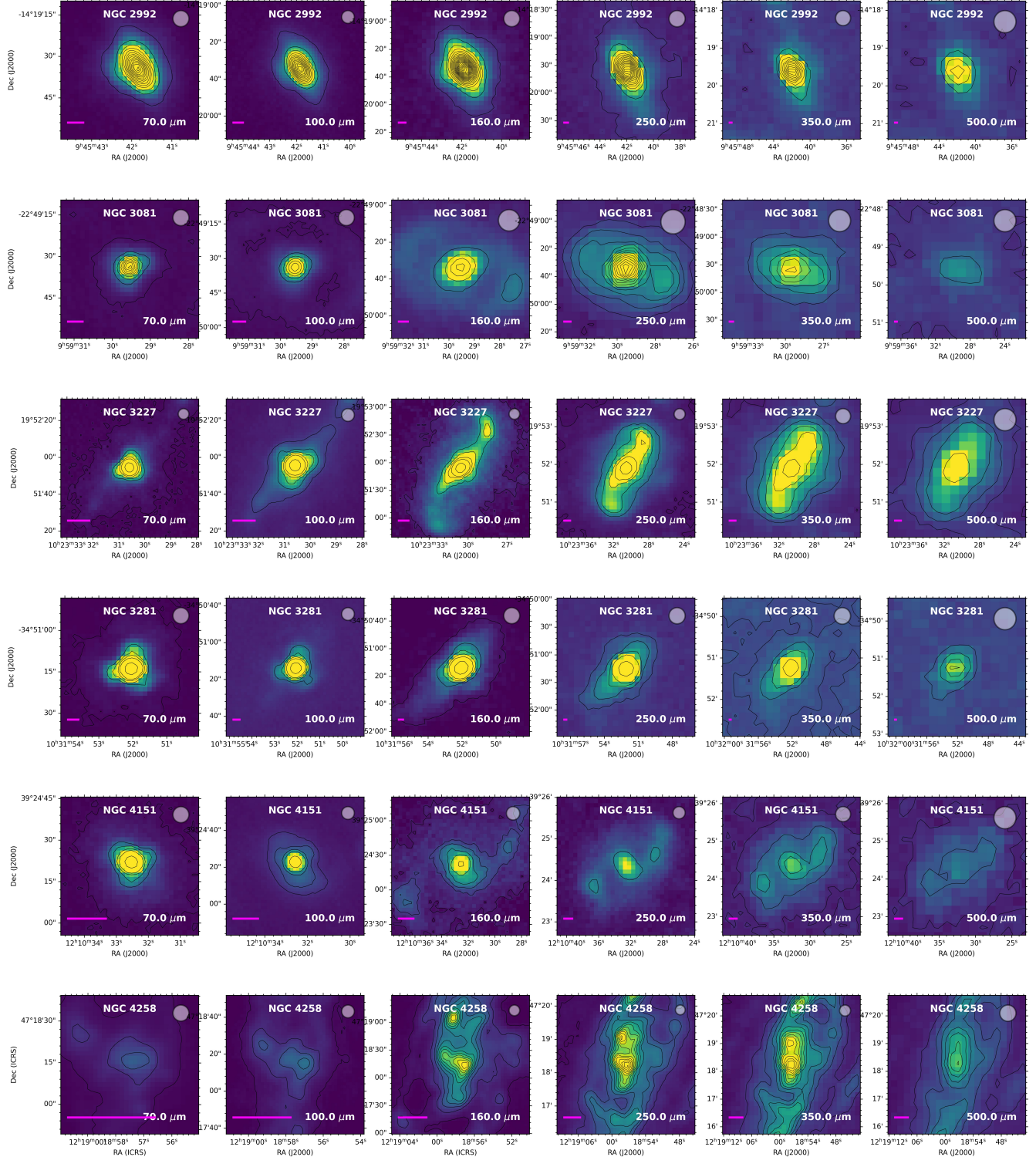
**Figure 11.** *Herschel* PACS and SPIRE FIR images. The white circle in the top right indicates the beam size of the observation, while the pink line in the bottom left indicates a distance of 1 kpc.

## B. BACKGROUND FITTING

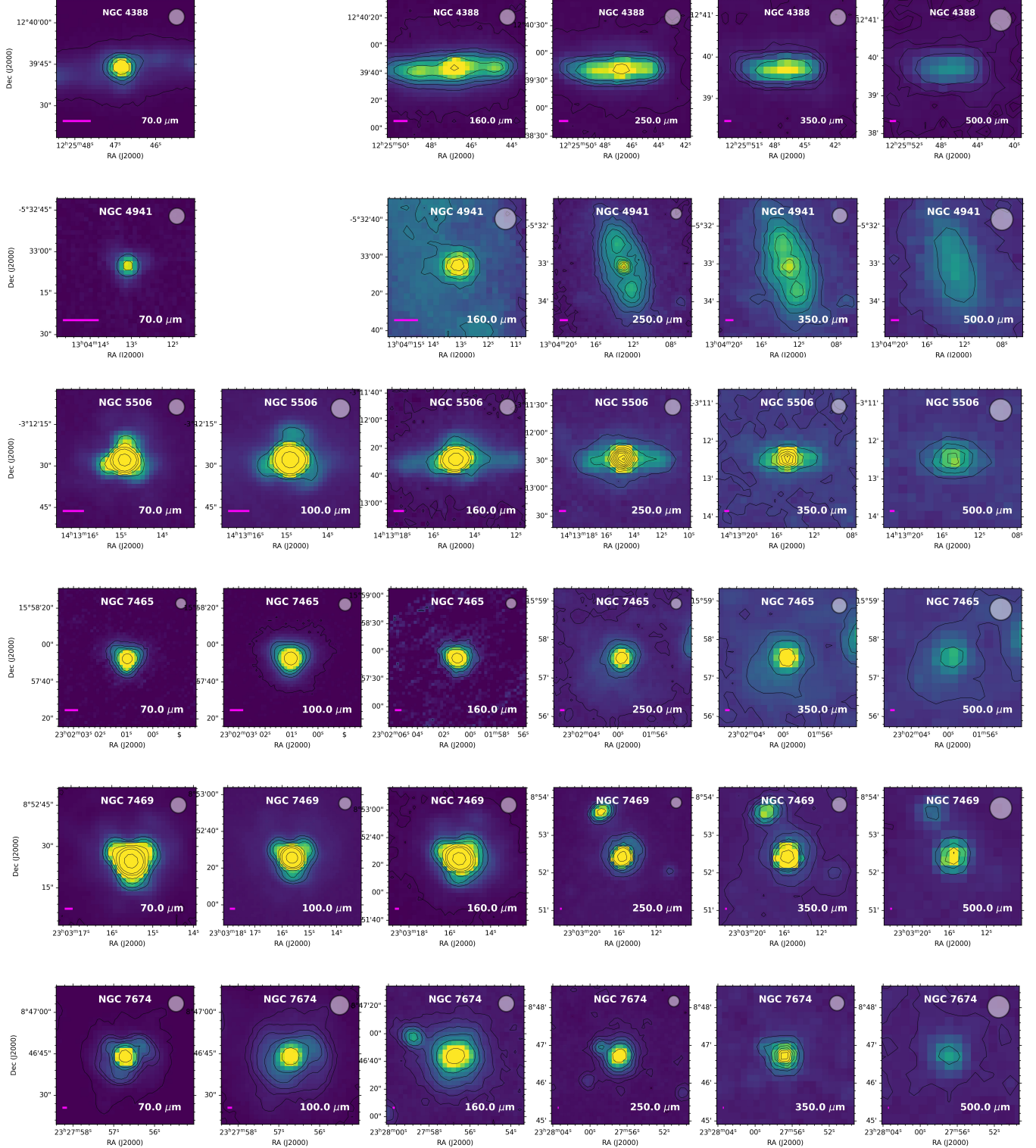
Figure 14 shows an example of the 2-D gaussian fitting we used to extract the central flux from the background of the host galaxy in wavelengths 30 - 500  $\mu\text{m}$ . The object used here is NGC 4388. In the first column, the original observation image is shown. The second column shows a model of the image using a PSF (Column 3) combined with the model background. Column 4 shows a PSF-subtracted image (Column 1 - Column 3) used to make the model background (Column 5). Column 6 shows the PSF- and background- subtracted image of the residuals.

## C. HOST GALAXY BACKGROUNDS - HERSCHEL

Here we show the results of PSF-subtracted images for objects in which only *Herschel* data showed host galaxy contamination.

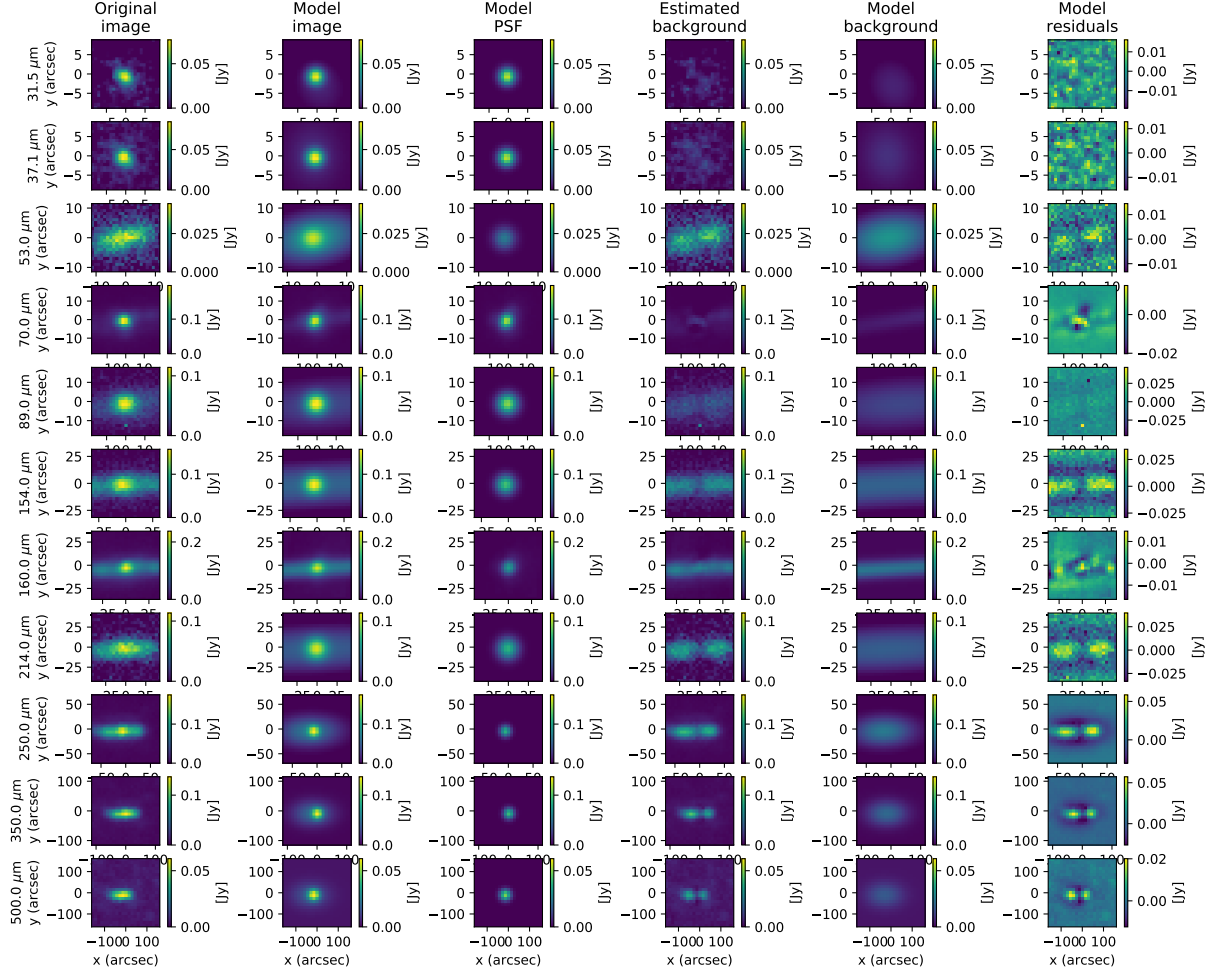


**Figure 12.** *Herschel* PACS and SPIRE FIR images. The white circle in the top right indicates the beam size of the observation, while the pink line in the bottom left indicates a distance of 1 kpc.



**Figure 13.** *Herschel* PACS and SPIRE FIR images. The white circle in the top right indicates the beam size of the observation, while the pink line in the bottom left indicates a distance of 1 kpc.

Fitting result - NGC4388 - best

**Figure 14.** Example of the 2D gaussian fitting routine explained in Section 4.1

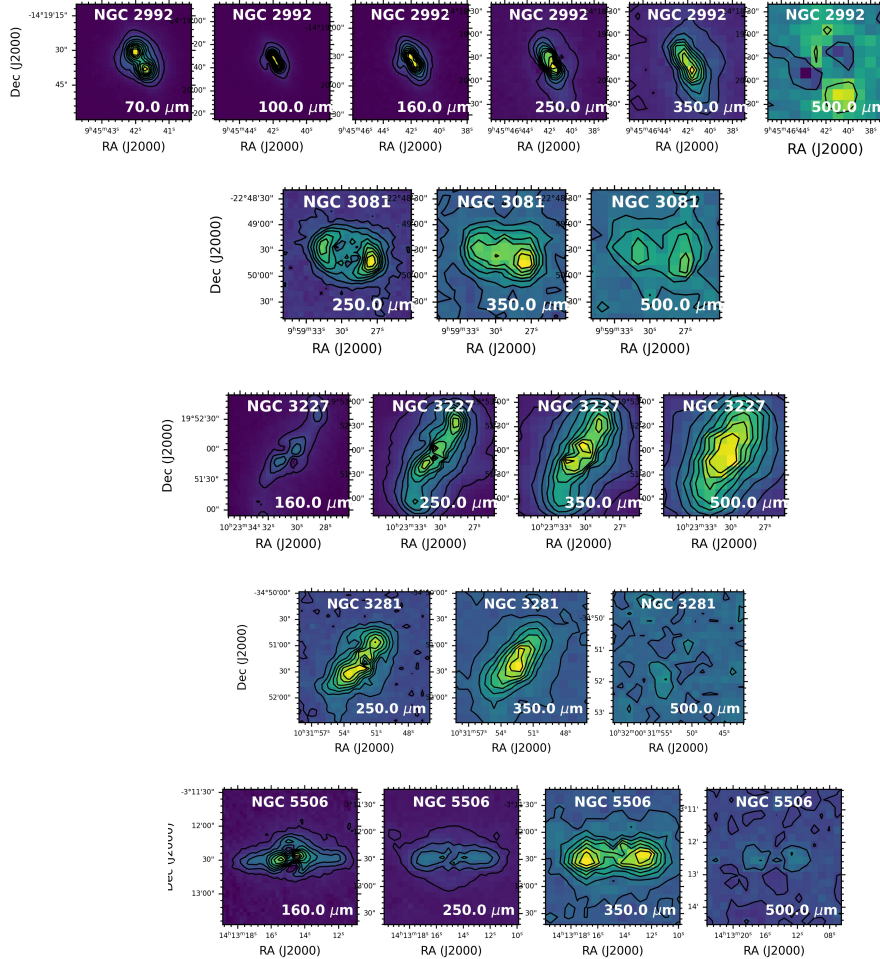


**Figure 15.** PSF-subtracted host galaxy images from archive *Herschel* data